Investigation of Nuclear Fragmentation and Neutral Pion Production with NA61/SHINE

Master's Thesis of

Johannes Bennemann

Karlsruhe Institute of Technology
Institute for Astroparticle Physics

First examiner:	Prof. Dr. Ralph Engel
Second examiner:	Prof. Dr. Ulrich Husemann
First advisor:	Dr. Michael Unger

15. September 2022 – 15. September 2023

Ich versichere wahrheitsgemäß, die Arbeit selbstständig verfasst, alle benutzten Quellen und Hilfsmittel vollständig und genau angegeben und alles kenntlich gemacht zu haben, was aus Arbeiten anderer unverändert oder mit Abänderungen entnommen wurde sowie die Satzung des KIT zur Sicherung guter wissenschaftlicher Praxis in der jeweils gültigen Fassung beachtet zu haben.

Als Prüfungsexemplar genehmigt von

. . . .

(Johannes Bennemann) (Prof. Dr. Ralph Engel)

Abstract

When cosmic rays travel through the Galaxy they interact with protons of the interstellar medium. These interactions fragment nuclei of heavier isotopes into lighter ones. The nuclear fragmentation cross sections required to model the propagation are measured with accelerator-based experiments. One of these experiments is the NA61/SHINE detector situated at the Super Proton Synchrotron at CERN. This thesis investigates various aspects of the measurement of nuclear interaction cross sections with NA61/SHINE. In particular, a method to separate interactions happening in different areas of the detector and an analytical description of the target is developed. They allow for a reduction of systematic uncertainties and the determination of the optimal target thickness.

Whereas cosmic rays of lower energies can be detected directly, ultra-high-energy cosmic rays (UHECR) have to be detected indirectly. When UHECRs hit the atmosphere, they initiate extensive air showers (EAS) that can be measured by ground-based detectors. The muon number predicted by EAS models does not match the observed muon number. This so-called muon puzzle can be solved by changing the energy distribution between the hadronic and electromagnetic components of the EAS. The hadronic component was previously measured by NA61/SHINE in π^-+C interactions at 158 GeV/c. This thesis analyzes the electromagnetic component of these interactions. A discrepancy of 30% between the measurement of electron-positron pairs and the model predictions is observed.

Zusammenfassung

Auf ihrem Weg durch die Galaxis wechselwirkt die kosmische Strahlung mit Protonen der interstellaren Materie. Dabei fragmentieren Kerne schwererer Isotope in leichtere. Die für die Modellierung des Transports kosmischer Strahlung benötigten Wirkungsquerschnitte der Fragmentation müssen in Beschleuniger-Experimenten gemessen werden. Ein solches Experiment ist der NA61/SHINE Detektor am *Super Positron Synchrotron* des CERNs. Diese Arbeit betrachtet verschiedene Aspekte der Messung von Fragmentationswirkungsquerschnitten mit NA61/SHINE. Insbesodere wird eine Methode entwickelt, um Wechselwirkungen in verschiedenen Bereichen des Detektors zu unterscheiden. Desweiteren wird ein analytisches Modell des Targets hergeleitet. Diese Methoden erlauben eine Reduktion systematischer Unsicherheiten und die Optimierung der Targetdicke.

Während niederenergetische kosmische Strahlung direkt detektiert werden kann, muss ultrahochenergetische kosmische Strahlung indirekt nachgewiesen werden. Hochenergetische kosmische Strahlung, welche auf die Atmosphäre trifft, löst ausgedehnte Luftschauer aus. Diese können von bodengestützten Detektoren gemessen werden. Die Anzahl der Myonen in diesen Schauern wird von den aktuellen Modellen nicht korrekt vorhergesagt. Dieses als Myonen Puzzle beschriebene Phänomen kann durch eine Änderung der Energieverteilung zwischen elektromagnetischer und hadronischer Komponente in Luftschauern erklärt werden. Letztere wurde 2009 von NA61/SHINE in π^-+C Kollisionen mit 185 GeV/c gemessen. Diese Arbeit analysiert die elektromagnetische Komponente dieser Kollisionen. Zwischen der Messung von Elektron-Positron-Paaren und der Modellvorhersage wird eine Abweichung von 30% festgestellt.

Contents

Abstract i

Zusammenfassung iii

Introduction 1

1 Cosmic Rays 3
- 1.1 Cosmic Ray Propagation . . . 5
- 1.2 Air Showers . . . 6

2 NA61/SHINE 9
- 2.1 SPS and H2 Beamline . . . 9
- 2.2 NA61/SHINE Detector . . . 10
- 2.3 Time Projection Chambers . . . 11

3 Nuclear Fragmentation in Carbon-Proton Interactions 13
- 3.1 Isotope Identification . . . 14
- 3.2 Extraction of Production Probabilities . . . 15
- 3.3 Boron Production Probabilities . . . 21
- 3.4 Analytical Description of the Target . . . 24
- 3.5 Target Thickness Optimization . . . 28

4 Neutral Pion Production in Pion-Carbon Interactions 35
- 4.1 Pair Production . . . 36
- 4.2 Source Particles . . . 40
- 4.3 Data and Reconstruction . . . 44
- 4.4 Particle Identification . . . 46
- 4.5 Invariant Mass Cut . . . 48
- 4.6 Corrections . . . 51
- 4.7 Results . . . 55

5 Summary 57

Bibliography 59

Acknowledgement 63

Introduction

Cataclysmic events in the universe – like the death of massive stars – leave behind extreme astrophysical environments. In such environments, the nuclei of the interstellar medium can be accelerated to high energies. These energetic particles are called cosmic rays. They propagate through the Galaxy along paths shaped by interstellar magnetic fields. When the cosmic ray nuclei pass through the interstellar medium, they interact with hydrogen nuclei and fragment into secondary isotopes. After a long journey, the primary and secondary cosmic rays reach the Earth, where they are detected by various instruments such as the spaceborne Alpha Magnetic Spectrometer (AMS) at the International Space Station. Spaceborne detectors are sensitive to the isotopic composition of cosmic rays. They yield valuable insights into the journey of cosmic rays through our Galaxy. Their detections are accompanied by laboratory measurements. At the Super Proton Synchrotron (SPS) at CERN, nuclei similar to those in cosmic rays are produced and their interactions with protons can be studied. To detect the secondary species, the hadron spectrometer NA61/SHINE is used. This experiment is capable of providing precise cross section measurements needed to understand the journey of cosmic rays. A pilot run was conducted in 2018 while new data is expected in 2024. In this thesis theoretical aspects of the measurement are considered in preparation for the next data taking.

Cosmic rays are not capable of penetrating the Earth's atmosphere. Nonetheless, the astroparticle physics community has overcome the challenge of ground-based cosmic ray detection. The detectors, like the Pierre Auger Observatory in Argentina, measure particle cascades initiated by nuclear interaction in the atmosphere. Due to their high energies – sometimes above 10^{20} eV – cosmic rays can produce billions of particles in the atmosphere. These Extensive Air Showers (EAS) can be examined with hadronic interaction models. While the models yield valuable insights into shower development, they fail to predict some important quantities. One of the largest discrepancies between measurements and simulations is the underprediction of the muon number in EAS. Again, laboratory experiments are required to understand the details of cosmic ray interactions. Since the SPS can provide beams of pions – the most common particle in EAS – π^-+C data was taken in 2009. In this thesis, an investigation of the potential of NA61 to measure the electromagnetic component in hadronic interactions is presented. This includes the measurement of the electron-positron pair spectrum originating mostly from neutral pion decays.

This thesis is organized as follows: After an introduction to cosmic rays in Chapter 1, a description of the detector NA61/SHINE follows in Chapter 2. The fragmentation experiment is discussed in Chapter 3, here two theoretical studies are performed in preparation for the experiment expected to take data in 2024. The first separates interactions happening inside the target from those happening in the material around it. In the second study, an analytical description of the processes inside the target is derived. Additionally, a method to optimize the target thickness is discussed.

The analysis of neutral pion production in π^--C interactions at 158 GeV is presented in Chapter 4. It is based on the identification of electron-positron pairs produced by photons. The photons themselves are decay products of neutral pions. How photon and pion spectra relate to the obtained electron-positron pair spectrum is discussed with theoretical considerations in mind. A first measurement of the electron-positron pair spectrum is presented. The thesis concludes with a summary in Chapter 5.

1 Cosmic Rays

Cosmic rays are charged particles that reach the Earth from outer space. 90% of cosmic rays are protons, 9% alpha particles and 1% heavier nuclei. Cosmic ray particles cover a wide range of energies up to 10^{20} eV. While the sources of cosmic rays are not fully known, most of them come from our Galaxy. This section will give a quick overview of cosmic ray properties and their detection. Unless otherwise noted, this section follows [1].

Figure 1.1 shows the energy spectrum of cosmic rays. Particles up to about 1 TeV can be detected in space by magnetic spectrometers. One experiment to point out is the Alpha Magnetic Spectrometer (AMS) on the International Space Station. AMS consists of a tracking system in a magnetic field to reconstruct particle momenta based on the bending of their tracks. Additionally, AMS contains a transition radiation detector and a Cherenkov detector to identify the particle. Further recent spaceborne cosmic ray experiments are the free-flying PAMELA and DAMPE satellites and CALET on the ISS.

Cosmic rays of higher energy cannot be detected by space-based detectors anymore. They are detected by ground-based experiments. In the atmosphere, cosmic rays trigger extensive air showers which are explained in Section 1.2. The particles in these air showers can be observed by fluorescence telescopes or water Cherenkov detectors. A notable experiment is the Pierre Auger Observatory in Argentina, which uses both fluorescence and Cherenkov detectors. It can observe cosmic rays up to the highest energies. A similar experiment covering the northern hemisphere is the Telescope Array in the United States.

Not only the energy spectrum, but the composition of cosmic rays is of interest. Cosmic rays consist of all elements up to iron, as expected from stellar element synthesis. But some elements, especially the light elements lithium, beryllium and boron, are more abundant than expected. Figure 1.2 shows the abundance of cosmic ray elements compared to the abundance in the solar system. The excess of light elements is caused by spallation processes in the Galaxy. They occur when cosmic ray nuclei collide with the interstellar medium and fragment into lighter nuclei. Spallation processes happen when cosmic rays travel through the Galaxy as described in Section 1.1.

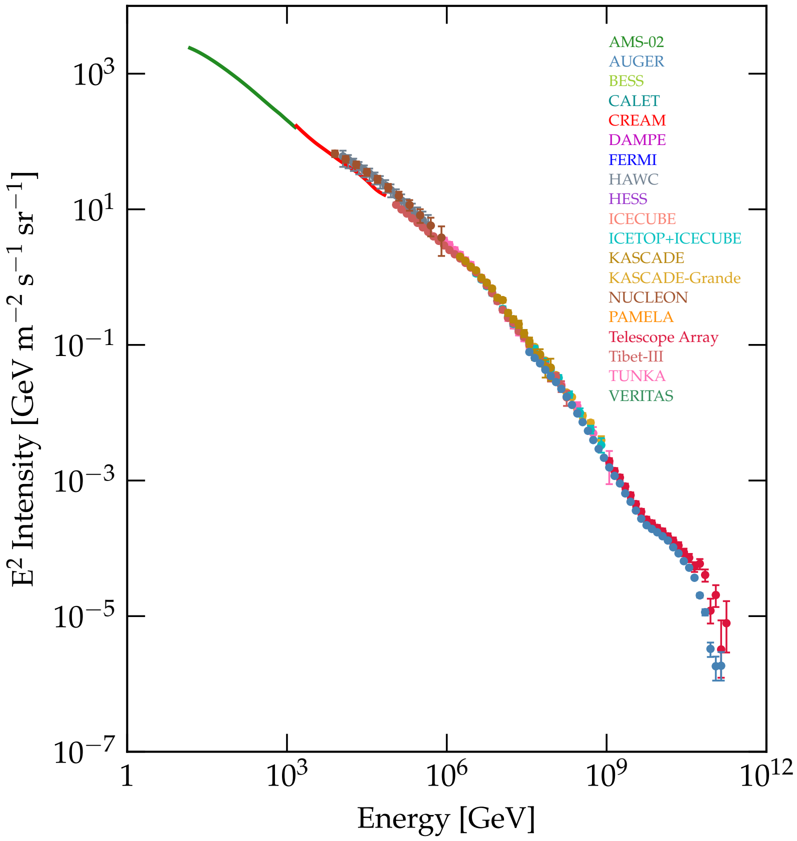

Figure 1.1: The energy spectrum of cosmic rays measured by different experiments. Modified from [2].

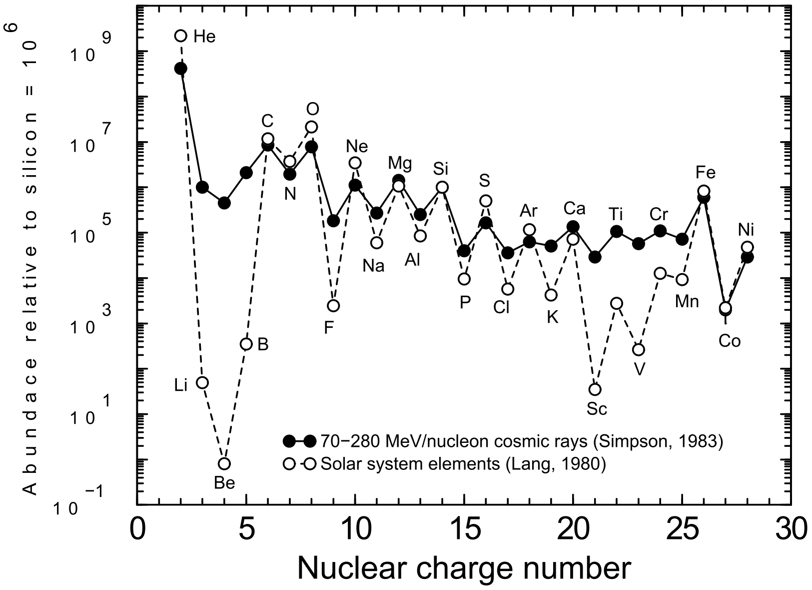

Figure 1.2: The abundance of cosmic ray elements compared to the abundance in the solar system. Taken from [3].

1.1 Cosmic Ray Propagation

The propagation of cosmic rays can be described by the diffusion-loss equation [4, p. 507]

$$\frac{\partial N_i}{\partial t} = D\,\nabla^2 N_i + \frac{\partial}{\partial E}(b(E)\,N_i) + Q_i - \frac{N_i}{\tau_i} + \sum_{j>i} \frac{P_{ji}}{\tau_j} N_j. \tag{1.1}$$

$N_i(E,t)$ is the number density of nuclei of species i. $D\,\nabla^2 N_i$ describes how particles enter and leave a specific volume element. This process is called diffusion with the diffusion coefficient D. $\frac{\partial}{\partial E}(b(E)\,N_i)$ describes how particles loose and gain energy. Considering an energy interval, this describes how many particles enter or leave this interval. $Q_i(E,t)$ is the source term. It describes how many particles are injected for each energy. $-N_i/\tau_i$ describes the destruction of nuclei by spallation processes. The spallation lifetime τ_i is the typical time a nucleus survives before it is fragmented. Since heavy nuclei fragment into lighter nuclei, they contribute to their number density. This is described by $P_{ji}\,N_j/\tau_j$ with the probability P_{ji} that a nuclei of species j fragments into a nuclei of species i.

As discussed in [4, Chapter 15], the diffusion-loss equation can be used to calculate the ratio between primary and secondary cosmic rays. Primary cosmic rays are nuclei accelerated by a cosmic ray source. Typical primary cosmic rays are carbon, oxygen and iron. These elements are produced in stellar nucleosynthesis [3]. Secondary cosmic rays are those produced in spallation reactions. For those secondary particles Eq. (1.1) can be simplified and written in terms of the traversed gas ξ,

$$\frac{\partial N_i(\xi)}{\partial \xi} = -\frac{N_i(\xi)}{\xi_i} + \sum_{j>i} \frac{P_{ji}}{\xi_j} N_j(\xi) \tag{1.2}$$

where $\xi = \rho v t$ with the density of the traversed gas ρ and the velocity v. ξ is called the traversed matter or grammage. As a model for the traversed path length and thus the grammage, they propose an exponential distribution of path lengths. This is motivated by the leaky box model. In this model, cosmic rays travel freely ($D = 0$) in a confined volume. They can leave the volume with a certain probability described by the characteristic escape time τ_e. This results in the differential equation

$$\frac{\partial N}{\partial t} = -\frac{N}{\tau_e}. \tag{1.3}$$

Written in grammage and integrated this results in

$$N \propto \exp(-\frac{\xi}{\xi_e}) \tag{1.4}$$

which is an exponential distribution. The ratio between primary cosmic ray nuclei of species i and its spallation products is

$$\frac{N_{\text{prod}}}{N_i} = \frac{1 - \exp(-\frac{\xi}{\xi_i})}{\exp(-\frac{\xi}{\xi_i})}. \tag{1.5}$$

This equation requires a good knowledge of ξ_i which depends on the fragmentation cross sections of the nuclei. How these cross sections can be measured is discussed in Chapter 3.

1.1.1 Useful Applications

The ratio of different cosmic ray isotopes can be used to calculate other useful quantities. One is the characteristic escape time τ_e of a cosmic ray nucleus, see Eq. (1.3). For a radioactive isotope, the relation between the lifetime τ_r and the escape time τ_e determines its abundance. The simplified transfer equation of radioactive nuclei is [4]

$$C_j - \frac{N_j}{\tau_e^j} - \frac{N_j}{\tau_r^j} - \frac{N_j}{\tau_s^j} = 0. \tag{1.6}$$

Here τ_s is the typical time in which a nucleus is destroyed by spallation and C its production rate. The ratio between a radioactive isotope j and a stable isotope i is

$$\frac{N_j}{N_i} = \frac{(\tau_e^i)^{-1} + (\tau_s^i)^{-1}}{(\tau_e^j)^{-1} + (\tau_r^j)^{-1} + (\tau_s^j)^{-1}} \frac{C_j}{C_i}. \tag{1.7}$$

Since the isotopic abundances are well known, measuring the production rate and spallation time enables us to calculate the escape time. Suitable for this calculation are the isotopes of beryllium. ^{10}Be has a half-life of 1.5 million years, which is in the order of magnitude of the escape time [4].

The propagation parameters derived from the ratio of primary and secondary cosmic rays apply to all cosmic rays. This includes antimatter like anti-protons and positrons. This can be used to search for dark matter annihilation [5]. The hypothetical WIMPs (Weakly Interacting Massive Particles) are expected to annihilate in the galactic dark matter halo. In this process, anti-protons are produced. The AMS detector does not only measure the isotopic composition of cosmic rays but also the antimatter flux. If the antimatter flux originates exclusively from secondary production, it will express the same propagation parameters as other cosmic rays. In the case of a primary contribution – like dark matter annihilation – its parameters would diverge from the expectation. Since the observed excess of the antimatter flux is small, a reduction of uncertainties of the cosmic ray propagation is necessary.

1.2 Air Showers

When cosmic rays hit the atmosphere, they interact with the nuclei of air molecules. In these interactions, various particles are created, which again interact with air nuclei. This results in a cascade of particles called an extensive air shower (EAS). To understand EAS, complex simulations are necessary. A typical EAS simulation framework is CORSIKA [6]. It uses hadronic interaction models to simulate nucleus-nucleus interactions and then

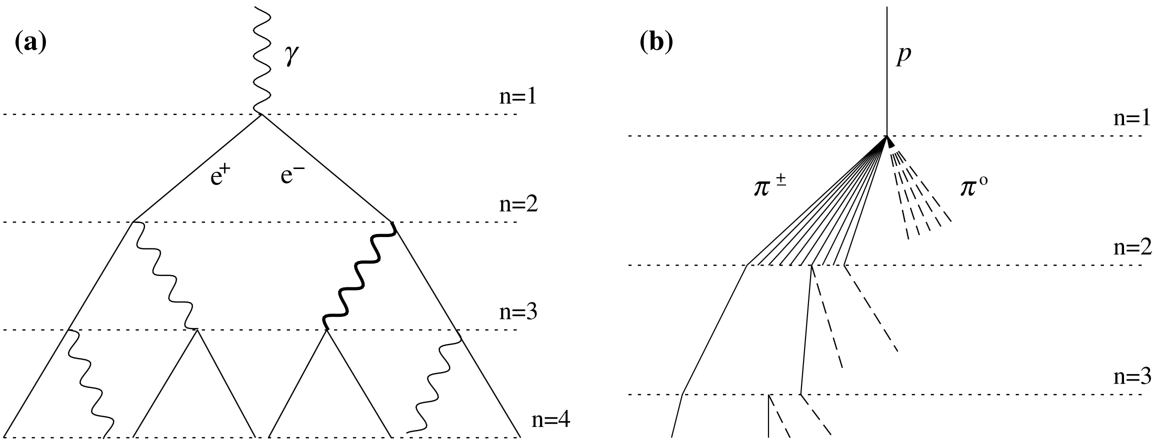

Figure 1.3: Illustrations of electromagnetic (a) and hadronic (b) showers. Taken from [7].

propagates the produced particles through the atmosphere. The models are Monte Carlo generators that are tuned to experimental data. They use theoretical models to extrapolate to higher energies.

It is instructive to look at an approximate theoretical description of air showers. Therefore, this section discusses a theoretical model developed by J. Matthews [7]. It extends an electromagnetic cascade model proposed by Heitler [8] to hadronic interactions.

Figure 1.3a illustrates how electromagnetic showers develop in the atmosphere. A photon interacts with an air molecule and produces an electron-positron pair. The electrons and positrons emit photons at regular intervals $d = \lambda_r \ln 2$. Here λ_r is the radiation length in the atmosphere. It is given in grams per square centimeter. This way the actual distance traveled can be calculated by multiplication with the density profile of the atmosphere. d is the distance in which the electron loses half of its energy as bremsstrahlung. Since this is a statistical process, it is obvious that the emission of one photon every d traveled is an approximation. It is assumed that each photon splits into an e^+e^- pair after traveling a distance d as well. In both cases, the energy is split in half in each step. Thus d is called the splitting length. This approximation allows many useful calculations.

The first thing one can calculate is the total shower size N. It is the sum of particles in the shower after n steps or a distance of $x = n\,\lambda_r \ln 2$. It can be calculated as

$$N = 2^n = e^{\frac{x}{\lambda_r}}. \tag{1.8}$$

Assuming the splitting ends when the energy loss from collisions gets larger than the radiative energy loss, there has to be a critical energy ξ_c^e where the shower reaches its maximum. With the initial photon energy E_0, the critical energy is reached when $E_0 = N\,\xi_c^e$ or after

$$n_c = \ln\left(\frac{E_0}{\xi_c^e}\right)\frac{1}{\ln 2} \tag{1.9}$$

splitting steps. This allows us to calculate the penetration depth X_{max} at which the shower reaches its maximum as

$$X_{\mathrm{max}} = n_c\,\lambda_r \ln 2 = \lambda_r \ln \frac{E_0}{\xi_c^e}. \tag{1.10}$$

While this model is pretty simple, it correctly describes the energy dependence of the shower size and the penetration depth.

Matthews transfers the Heitler model to hadronic showers. As before interactions happen in regular intervals of length $d = \lambda_I \ln 2$, as illustrated in Fig. 1.3b. Here λ_I is the interaction length of charged pions in the atmosphere. It is assumed that each interaction produces N_{ch} charged pions. Additionally, $\frac{1}{2}N_{\mathrm{ch}}$ neutral pions are produced. These immediately decay into photons and initiate electromagnetic showers. The critical energy ξ_c^π is now the energy at which the decay length becomes smaller than the interaction length. At this energy pions decay into muons before they can initiate a new interaction. With this, the number of interactions needed to reach the maximum can be calculated as

$$E_\pi = \frac{E_0}{\left(\frac{3}{2}N_{\mathrm{ch}}\right)^{n_c}} \overset{!}{=} \xi_c^\pi \implies n_c = \ln\left(\frac{E_0}{\xi_c^\pi}\right)\frac{1}{\ln\left(\frac{3}{2}N_{\mathrm{ch}}\right)}. \tag{1.11}$$

Since the pions decay into muons after reaching the maximum, the muon number can be calculated as

$$N_\mu = (N_{\mathrm{ch}})^{n_c}\,. \tag{1.12}$$

At each step, electromagnetic showers can be added for each neutral pion produced. This allows the calculation of the shower maximum and the penetration depth. A rough approximation of the penetration depth of a proton-induced shower is

$$X_{\mathrm{max}}^p = X_0 + X_{\mathrm{max}}^\gamma - \lambda_r \ln(3N_{\mathrm{ch}})\,. \tag{1.13}$$

Here X_0 is the depth of the initial interaction and X_{max}^γ is the depth of the corresponding electromagnetic shower.

An important observation is that the predicted number of muons does not match the measurements [9]. The same is true for Monte Carlo simulations. This is called the muon puzzle. Equations (1.11) and (1.12) suggest two options to change the muon number. The first is to change the number of charged pions N_{ch} produced in each interaction. The second is to change the split between charged and neutral pions. Let the total number of pions be N_π. It can be calculated from N_{ch} as

$$N_\pi = N_{\mathrm{ch}} + f\,N_{\mathrm{ch}} = (1+f)N_{\mathrm{ch}}. \tag{1.14}$$

In the original model $f = \frac{1}{2}$. With an arbitrary f, Eq. (1.11) changes to

$$n_c = \ln\left(\frac{E_0}{\xi_c^\pi}\right)\frac{1}{\ln\left((1+f)N_{\mathrm{ch}}\right)}. \tag{1.15}$$

Both options require a better understanding of pion-nucleus interactions. A method to analyze neutral pion production is discussed in Chapter 4.

2 NA61/SHINE

The experiments in this thesis are performed at the NA61/SHINE detector at CERN. NA61 is located at the H2 beamline of the CERN North Area, thus the name NA61. SHINE stands for SPS Heavy Ion and Neutrino Experiment. This chapter will introduce the detector, its beamline and the accelerator. Additionally, the functionality of the most important detector part for the analysis, the time projection chamber, is discussed. Unless otherwise noted all information in this chapter is from [10].

2.1 SPS and H2 Beamline

The Super Proton Synchrotron (SPS) is a proton and heavy-ion accelerator at CERN. It has a circumference of 6.8 km and is supplied with protons and ions from the Proton Synchrotron (PS). The PS has a circumference of 628 m. It accelerates protons to 14 GeV/c. The protons are then injected into the SPS and further accelerated up to 400 GeV/c.

Additionally, the PS can accelerate lead ions provided by the Low Energy Ion Ring (LEIR). The ions are accelerated to 5.9 GeV per nucleon before injection into the SPS. Lead ions can be accelerated up to 160 GeV per nucleon in the SPS.

Figure 2.1 shows the entire acceleration chain for protons and lead ions. After the acceleration, the proton or ion beam is delivered to the CERN North Area.

NA61 is situated at the H2 beamline. In an underground cavern, multiple beryllium plates are available to be used a the T2 target. This target is used to produce secondary particles like lighter ions or charged hadrons. After the T2 target, a spectrometer is used to separate the produced particles by rigidity. Since rigidity is momentum per charge, ions of different masses can pass the spectrometer. The separation of those ions is discussed in Section 3.1.

Different hadrons can be identified by the Cherenkov Differential Counter with Achromatic Ring Focus (CEDAR). It is filled with pressurized gas in which passing particles emit Cherenkov radiation. The light is then collected by photomultiplier tubes which serve as beam trigger. By changing the gas pressure and the optical system the wanted hadron species can be selected.

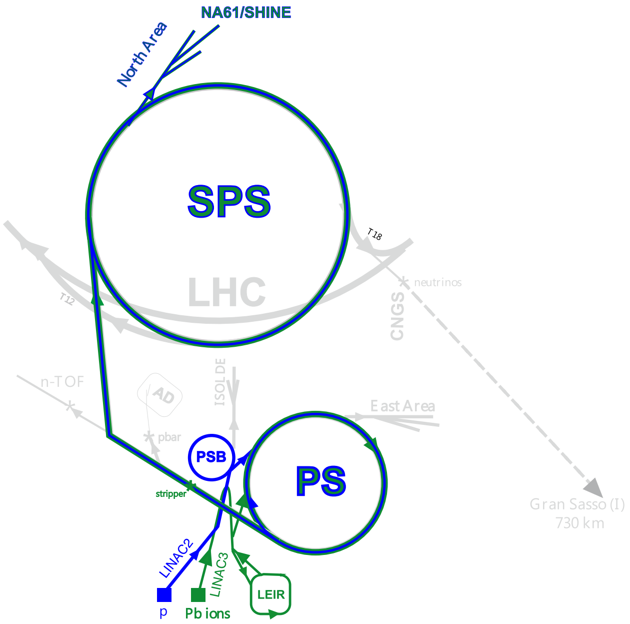

Figure 2.1: The acceleration chains for protons (blue) and ions (green) consist of multiple accelerators. Both chains start with linear accelerators (LINAC2/3) followed by either the Proton Synchrotron Booster (PSB) or the Low Energy Ion Ring (LEIR). After injection into the PS, both chains follow the same path. Taken from [10].

2.2 NA61/SHINE Detector

NA61 consists of five time projection chambers (TPC). Their arrangement can be seen in Fig. 2.2. The two Vertex TPCs (VTPC-1/2) are located inside a magnetic field. To create the field each VTPC is surrounded by a superconducting dipole magnet. The magnets are 5.7 m wide, 3.6 m long and operate at 1.5 T and 1.1 T. Between the magnets, the GAP-TPC is located in the beamline.

Downstream of the VTPCs, there are the two Main TPCs (MTPC-L/R) placed left and right of the beamline. Each MTPC is 3.9 m wide and long with a height of 1.8 m. Upstream of the VTPCs is the target. Before the target, there are several beam detectors. They include the aforementioned CEDAR as well as multiple Beam Position Detectors (BPD-1/2/3). These are proportional wire chambers filled with gas and a wire lattice. They allow reconstructing the path of a beam particle that ionizes the gas.

Additionally, multiple scintillators are located upstream of the target. They can be used as trigger (S1/S2) and veto (V0/V1/V1') detectors. The latter have a hole where the beam particle can pass through. There is another scintillator between the VTPCs. This detector is called S4 and is used as an interaction trigger.

NA61 allows for different trigger modes. Up to four triggers can be defined simultaneously. The triggers can be pre-scaled, which means that they only accept every nth event.

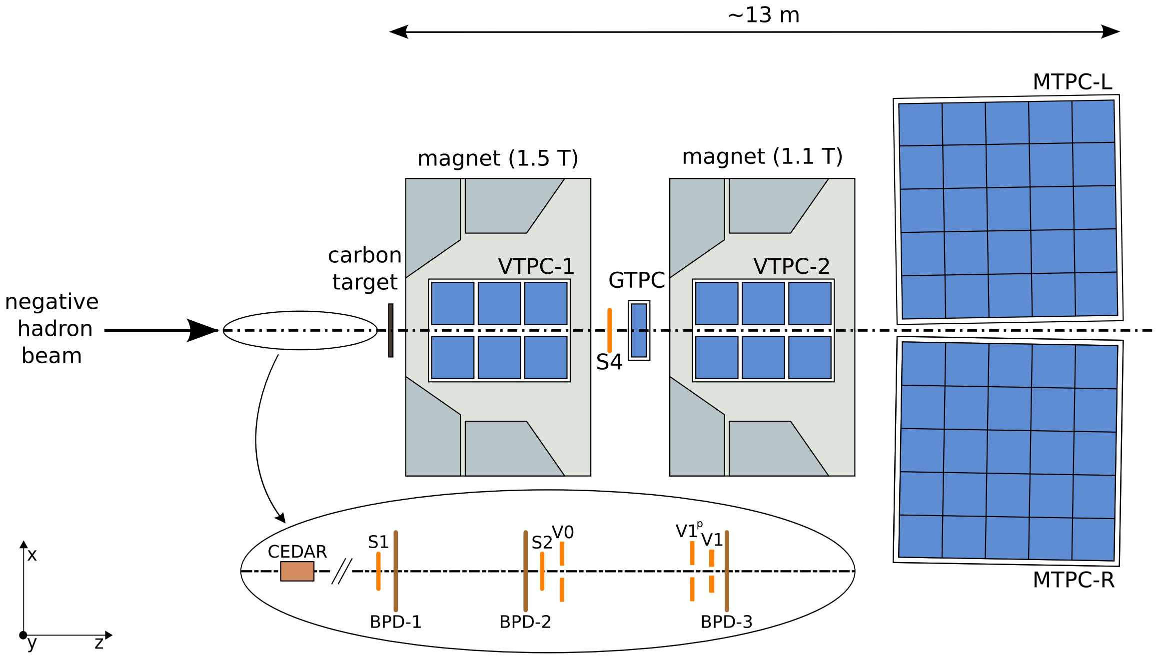

Figure 2.2: Detector layout as used in the 2009 $\pi^- + \mathrm{C}$ run. Taken from [11].

Common triggers are the beam trigger, also called the zero bias trigger, and the interaction trigger. The beam trigger is defined as S1 and S2 hit, V0, V1 and V1' not hit. This trigger accepts all events in which a beam particle hits the target. When a beam particle passes the target without interaction, it hits S4. Thus the interaction trigger uses S4 as an additional veto detector.

2.3 Time Projection Chambers

When charged particles travel through gas, they ionize the gas molecules and leave a trail of ionization electrons. In a time projection chamber (TPC) these trails are measured. NA61 uses TPCs filled with a mixture of argon and carbon dioxide. The gas volume is surrounded by a field cage of aluminized Mylar strips. High voltage is applied to the strips to create a uniform electric field. Ionization electrons in the field drift upwards with a constant velocity.

At the top of the TPCs, there are proportional wire chambers that amplify and detect the drifting electrons. The chambers are divided into pads with an area of about 1 cm^2. This allows a two-dimensional readout of the TPC. The charge deposit in each pad is stored continuously and contains the arrival time information. With the drift velocity, the vertical position of the track can be calculated from the arrival time. Thus a three-dimensional reconstruction of an ionization trail in the TPC is possible.

The reconstruction of particle tracks is a core task of NA61. Inside the magnetic field, the tracks are bent inversely proportional to their momentum. Thus the bending of the tracks can be used to measure the momentum of the particle.

The charge deposit is proportional to the number of ionization electrons and thus the energy loss of the particle. Since the relation between energy loss and momentum depends on the particle species, the energy loss can be used to identify the particle. In Section 4.4 the particle identification with this method is discussed.

3 Nuclear Fragmentation in Carbon-Proton Interactions

The original topic of this thesis was the measurement of fragmentation cross sections of cosmic ray nuclei. The measurement itself was delayed to a date after the end of this thesis. This chapter discusses two theoretical studies performed as preparations for the measurement. In 2018 a pilot run of the measurement was carried out [12, 13]. The cross sections for the fragmentation of ^{12}C to ^{11}C, ^{11}B and ^{10}B were published recently [14, 15].

As discussed in Section 1.1, cosmic rays traveling through the Galaxy interact with the nuclei of the interstellar medium. Thus heavier nuclei can fragment into lighter nuclei. To utilize this process for the understanding of cosmic ray propagation, the cross sections of cosmic ray nuclei with hydrogen are needed. The importance of such measurements is discussed in [16, 17].

For the measurement, a beam of different nuclei is produced by the fragmentation of lead ions. Lead ions are accelerated by the SPS and fragmented at the T2 target, see Section 2.1. The nuclei are selected by rigidity and transported to NA61. There they hit one of two targets. Since setup and control of a liquid hydrogen target are non-trivial, a polyethylene and a carbon target are used instead. Polyethylene consists of hydrogen and carbon atoms. Thus a measurement with polyethylene yields a combined hydrogen-carbon cross section. The carbon target is used to measure the carbon cross section and eliminate it from the polyethylene cross section. With this method, the hydrogen cross section can be determined.

The measurement consists of two isotope identifications. One performed before and one after the target. These are discussed in Section 3.1. Not all fragmentation reactions happen inside the target. Contributions from upstream and downstream materials have to be considered as well. How to extract the production probabilities inside the target is discussed in Section 3.2. One of the most important observables to understand cosmic ray propagation in the Galaxy is the boron to carbon ratio. Thus the developed method is applied to the production of boron in Section 3.3. To describe the processes inside the target a mathematically rigorous formalism is developed in Section 3.4. Additionally, an application of the developed formalism – the optimization of the target thickness – is presented in Section 3.5.

3.1 Isotope Identification

For the experiment, a similar setup as was shown in Fig. 2.2 is used. The most important differences are the absence of S4 and CEDAR as well as an additional scintillator A. The A detector is placed 240 m upstream of the S1 detector. The A and S1 detectors are used for the upstream isotope identification, see Section 3.1.1. Downstream of the target, the isotopes are identified by their tracks in the MTPC-L, see Section 3.1.2.

3.1.1 Upstream

To identify an isotope, the charge q and the mass m of an ion have to be measured. The charge of an ion is the elementary charge e times the charge number Z. Its mass is approximately the proton mass m_p times the atomic mass number A. The charge deposit and thus the signal strength in a scintillator is proportional to Z^2. Thus the charge number can be measured with the scintillators. The ions provided by the H2 beamline have a known rigidity $R = p/q$. Knowing the charge of the ion, its momentum p can be calculated from the rigidity.

To obtain the mass, the relation between momentum and mass can be used,

$$m = \frac{p}{\gamma v} \qquad \text{with} \qquad \gamma = \left(1 - \frac{v^2}{c^2}\right)^{-\frac{1}{2}} . \tag{3.1}$$

The velocity v can be measured with a time-of-flight measurement. For this, the time difference between the A and S1 detectors is used. With the charge and mass measurements, the charge number Z and the atomic mass number A can be calculated. Thus different isotopes can be identified. More details on the upstream isotope identification can be found in [12].

3.1.2 Downstream

After the target, the tracks of the ion are bent by the magnetic field. Since all ions are positively charged, all ion tracks traverse the MTPC-L. As in the scintillators, the energy loss $\frac{dE}{dx}$ in a TPC is proportional to Z^2. Thus the charge q and charge number Z of the ion can be calculated from the energy loss. The bending of the tracks depends on the rigidity. Since the momentum per nucleon is approximately conserved in nuclear fragmentation, the rigidity changes when the mass of an ion changes in an interaction. Thus ions with different masses will end up at different positions in the MTPC. The difference Δx between a fragmented ion and a beam particle was analyzed in [14]. The distribution of Δx for boron ($Z = 5$) in the pilot run is shown in Fig. 3.1. The number of isotopes with an atomic mass number A is obtained by a fit.

Ions that fragment inside of the magnetic field are bent with two rigidities, one before and one after the interaction. This results in their tracks being between the tracks of their

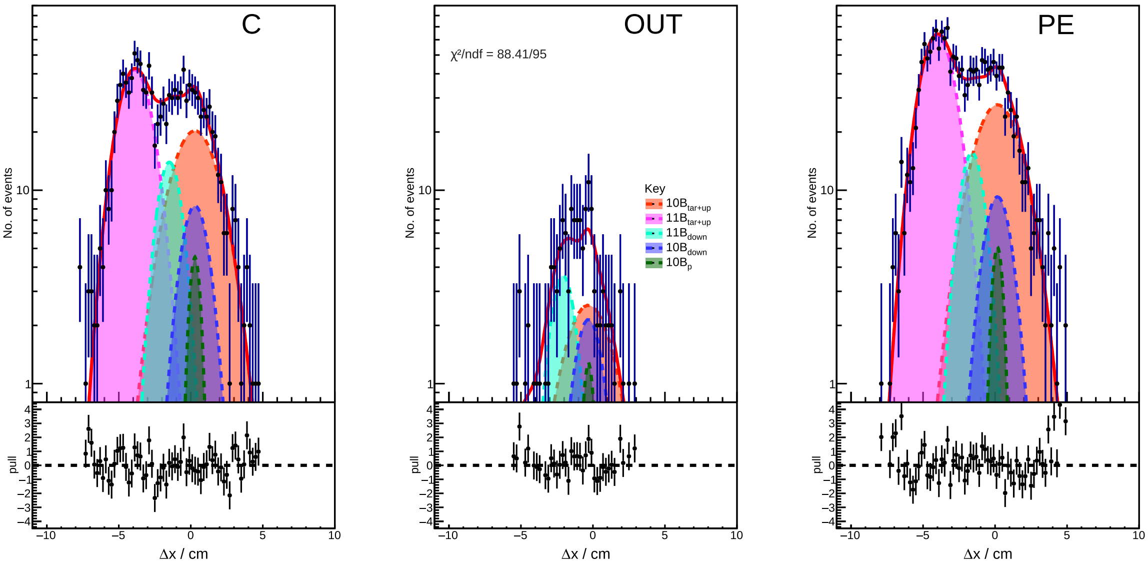

Figure 3.1: The distribution of boron ($Z = 5$) fragment positions. The left side with the carbon target inserted, the right side with the polyethylene target and the middle without a target. The pink and orange fits are ^{11}B and ^{10}B ions produced upstream and in the target. The cyan and blue fits are ions produced inside the magnetic field. The green peak is from primary ^{10}B that passed the upstream ^{12}C selection. Taken from [14].

initial and final masses. The fits in Fig. 3.1 can identify these ions. Ions that fragment downstream of VTPC-2, i.e. after they traversed the magnetic field, end up at the same position as they would have without the fragmentation. However, ions that fragment before the target cannot be distinguished from ions fragmenting inside the target.

3.2 Extraction of Production Probabilities

The methods described in Section 3.1 identify ions in the beam and the detector. For the analysis, the number of ions entering and leaving the target is required. Since the ions can interact anywhere between the S1 detector and the MTPC-L, the measured numbers are not the required numbers. To calculate the numbers for the target, an additional measurement without the target inserted is conducted. The two measurements are called the target-in and target-out measurements. In this section, the numbers from the isotope identification are converted into the target numbers.

To clarify the notation in this chapter, everything is expressed in probabilities with a superscript and two subscripts:

$$P^{\text{area}}_{\text{A}\to\text{B}} \tag{3.2}$$

The superscript specifies the area of the detector in which the probability is considered. The special areas “in” and “out” denote the probabilities along the entire detector in the target-in and target-out cases. The subscripts specify the incoming and outgoing particles. An “X” denotes everything that is not explicitly specified. For example $P^{\mathrm{tar}}_{^{12}\mathrm{C}\to{}^{11}\mathrm{C}}$ is the probability that a ^{12}C nucleus enter the target and a ^{11}C nucleus leaves the target.

In the following, the extraction method is applied to the production of ^{11}C from ^{12}C. ^{11}C is unstable and decays into ^{11}B with a half-life of 20 minutes. Thus it contributes to the total boron production. The more complex direct boron production is calculated in Section 3.3.

3.2.1 Carbon-12 Interactions

A Carbon-12 beam results in four signals in the MTPC-L:

1. ^{12}C that passes the detector without interaction
2. ^{11}C that is produced before entering the magnetic field
3. ^{11}C that is produced inside the magnetic field
4. fragments with $Z < 6$ or $A < 11$

The ^{11}C produced inside the magnetic field does not end up at the same position as the ^{11}C produced in the target or upstream. This is due to the mass and thus rigidity change which affects the trajectory in the magnetic field.
There are three areas in which interactions can take place:

1. before the target, denoted as $^{\mathrm{up}}$ (upstream)
2. inside the target, denoted as $^{\mathrm{tar}}$ (target)
3. inside the magnetic field, denoted as $^{\mathrm{down}}$ (downstream)

In Fig. 3.2 an overview of all probabilities is shown. All probabilities in one box add up to one due to the conservation of probability. Following a path through the diagram and multiplying all probabilities yields the probability of that path. When two paths join, their probabilities can be added together to get the combined probability. This method can be used to construct all relevant equations. In the following this construction is shown for primary ^{12}C with and without target inserted. In Section 3.2.2 the same construction is shown for primary ^{11}C. By combining both calculations, the ^{11}C production probability in the target can be obtained.

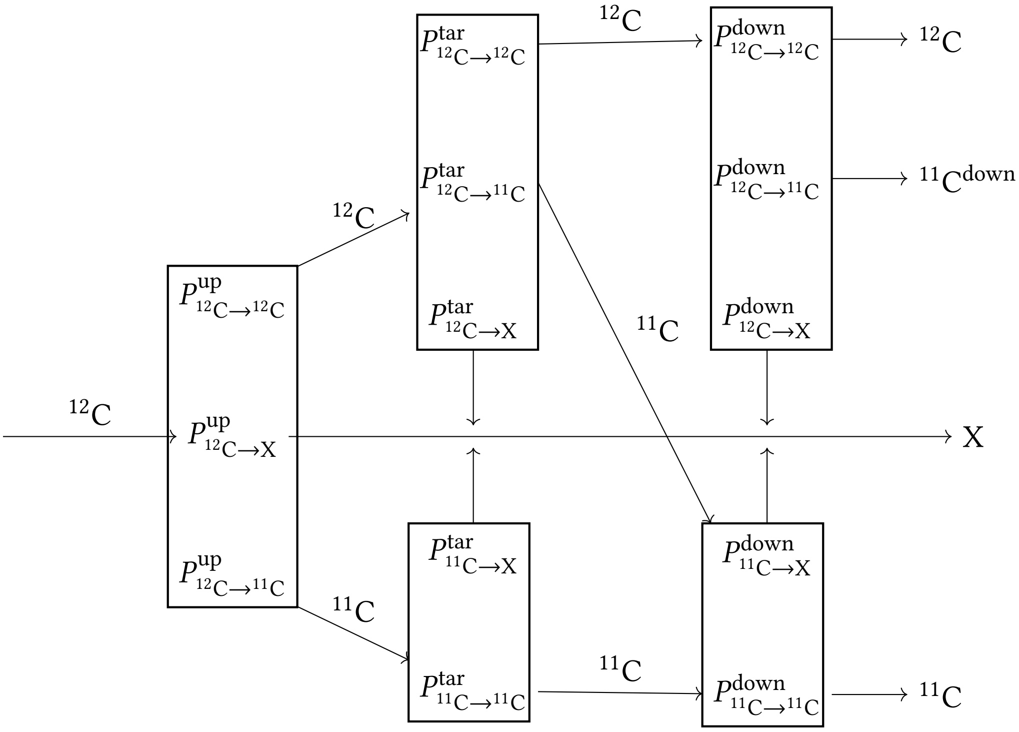

Figure 3.2: Graphical representation of the probability calculations.

Calculation with Target

The upstream survival probability of ^{12}C is

$$P^{\text{up}}_{^{12}\text{C}\to{}^{12}\text{C}} = 1 - P^{\text{up}}_{^{12}\text{C}\to{}^{11}\text{C}} - P^{\text{up}}_{^{12}\text{C}\to\text{X}} \tag{3.3}$$

where X denotes everything except ^{12}C and ^{11}C. Likewise, the probability that ^{12}C passes the target is

$$P^{\text{tar}}_{^{12}\text{C}\to{}^{12}\text{C}} = 1 - P^{\text{tar}}_{^{12}\text{C}\to{}^{11}\text{C}} - P^{\text{tar}}_{^{12}\text{C}\to\text{X}}. \tag{3.4}$$

and the probability that ^{12}C passes the magnetic field is

$$P^{\text{down}}_{^{12}\text{C}\to{}^{12}\text{C}} = 1 - P^{\text{down}}_{^{12}\text{C}\to{}^{11}\text{C}} - P^{\text{down}}_{^{12}\text{C}\to\text{X}}. \tag{3.5}$$

These probabilities can be read from the boxes in Fig. 3.2. By tracing down the path for ^{12}C, the measured survival probability of ^{12}C is obtained as

$$P^{\text{in}}_{^{12}\text{C}\to{}^{12}\text{C}} = P^{\text{up}}_{^{12}\text{C}\to{}^{12}\text{C}}\, P^{\text{tar}}_{^{12}\text{C}\to{}^{12}\text{C}}\, P^{\text{down}}_{^{12}\text{C}\to{}^{12}\text{C}}. \tag{3.6}$$

The probability for the measured ^{11}C production is

$$P^{\text{in}}_{^{12}\text{C}\to{}^{11}\text{C}} = P^{\text{up}}_{^{12}\text{C}\to{}^{11}\text{C}}\, P^{\text{tar}}_{^{11}\text{C}\to{}^{11}\text{C}}\, P^{\text{down}}_{^{11}\text{C}\to{}^{11}\text{C}} + P^{\text{up}}_{^{12}\text{C}\to{}^{12}\text{C}}\, P^{\text{tar}}_{^{12}\text{C}\to{}^{11}\text{C}}\, P^{\text{down}}_{^{11}\text{C}\to{}^{11}\text{C}}. \tag{3.7}$$

The first term describes the upstream production. The second term describes the production inside the target. Both contain the downstream survival probability of ^{11}C. The production of ^{11}C inside the magnetic field is

$$P^{\mathrm{in}}_{^{12}\mathrm{C}\to{}^{11}\mathrm{C}^{\mathrm{down}}} = P^{\mathrm{up}}_{^{12}\mathrm{C}\to{}^{12}\mathrm{C}}\,P^{\mathrm{tar}}_{^{12}\mathrm{C}\to{}^{12}\mathrm{C}}\,P^{\mathrm{down}}_{^{12}\mathrm{C}\to{}^{11}\mathrm{C}}. \tag{3.8}$$

Finally, the production of everything else is

$$\begin{aligned}P^{\mathrm{in}}_{^{12}\mathrm{C}\to\mathrm{X}} = {} & P^{\mathrm{up}}_{^{12}\mathrm{C}\to\mathrm{X}}\\ & + P^{\mathrm{up}}_{^{12}\mathrm{C}\to{}^{12}\mathrm{C}}\,P^{\mathrm{tar}}_{^{12}\mathrm{C}\to\mathrm{X}}\\ & + P^{\mathrm{up}}_{^{12}\mathrm{C}\to{}^{11}\mathrm{C}}\,P^{\mathrm{tar}}_{^{11}\mathrm{C}\to\mathrm{X}}\\ & + P^{\mathrm{up}}_{^{12}\mathrm{C}\to{}^{12}\mathrm{C}}\,P^{\mathrm{tar}}_{^{12}\mathrm{C}\to{}^{12}\mathrm{C}}\,P^{\mathrm{down}}_{^{12}\mathrm{C}\to\mathrm{X}}\\ & + P^{\mathrm{up}}_{^{12}\mathrm{C}\to{}^{11}\mathrm{C}}\,P^{\mathrm{tar}}_{^{11}\mathrm{C}\to{}^{11}\mathrm{C}}\,P^{\mathrm{down}}_{^{11}\mathrm{C}\to\mathrm{X}}\\ & + P^{\mathrm{up}}_{^{12}\mathrm{C}\to{}^{12}\mathrm{C}}\,P^{\mathrm{tar}}_{^{12}\mathrm{C}\to{}^{11}\mathrm{C}}\,P^{\mathrm{down}}_{^{11}\mathrm{C}\to\mathrm{X}}.\end{aligned} \tag{3.9}$$

The first term describes the upstream destruction of ^{12}C. The second and third terms describe the destruction of ^{12}C and ^{11}C in the target. The fourth term describes the downstream destruction of ^{12}C. The last two terms describe the downstream destruction of ^{11}C which was produced upstream or in the target.

Calculation without Target

When taking data without a target inserted, the upstream and downstream probabilities remain unchanged. Thus the probability of surviving the target is

$$P^{\mathrm{tar,out}}_{^{12}\mathrm{C}\to{}^{12}\mathrm{C}} = 1. \tag{3.10}$$

All other target probabilities vanish. Thus Eq. (3.6) changes to

$$P^{\mathrm{out}}_{^{12}\mathrm{C}\to{}^{12}\mathrm{C}} = P^{\mathrm{up}}_{^{12}\mathrm{C}\to{}^{12}\mathrm{C}}\,P^{\mathrm{down}}_{^{12}\mathrm{C}\to{}^{12}\mathrm{C}}. \tag{3.11}$$

It can be used to eliminate upstream and downstream probabilities,

$$\frac{P^{\mathrm{in}}_{^{12}\mathrm{C}\to{}^{12}\mathrm{C}}}{P^{\mathrm{out}}_{^{12}\mathrm{C}\to{}^{12}\mathrm{C}}} = P^{\mathrm{tar}}_{^{12}\mathrm{C}\to{}^{12}\mathrm{C}}. \tag{3.12}$$

Equation (3.7) changes to

$$P^{\mathrm{out}}_{^{12}\mathrm{C}\to{}^{11}\mathrm{C}} = P^{\mathrm{up}}_{^{12}\mathrm{C}\to{}^{11}\mathrm{C}}\,P^{\mathrm{down}}_{^{11}\mathrm{C}\to{}^{11}\mathrm{C}}. \tag{3.13}$$

In this case, only the downstream probability can be eliminated,

$$\frac{P^{\mathrm{in}}_{^{12}\mathrm{C}\to{}^{11}\mathrm{C}}}{P^{\mathrm{out}}_{^{12}\mathrm{C}\to{}^{11}\mathrm{C}}} = P^{\mathrm{tar}}_{^{11}\mathrm{C}\to{}^{11}\mathrm{C}} + \frac{P^{\mathrm{up}}_{^{12}\mathrm{C}\to{}^{12}\mathrm{C}}}{P^{\mathrm{up}}_{^{12}\mathrm{C}\to{}^{11}\mathrm{C}}}\,P^{\mathrm{tar}}_{^{12}\mathrm{C}\to{}^{11}\mathrm{C}}. \tag{3.14}$$

The probability $P^{\mathrm{tar}}_{^{11}\mathrm{C}\to{}^{11}\mathrm{C}}$ can be calculated from measurements with primary ^{11}C similar to Eq. (3.12), see Section 3.2.2. The probability $P^{\mathrm{up}}_{^{12}\mathrm{C}\to{}^{11}\mathrm{C}}$ in the denominator is small. If it is not well known, this calculation should be avoided. How to calculate the ^{11}C production probability otherwise is discussed in Section 3.2.3.

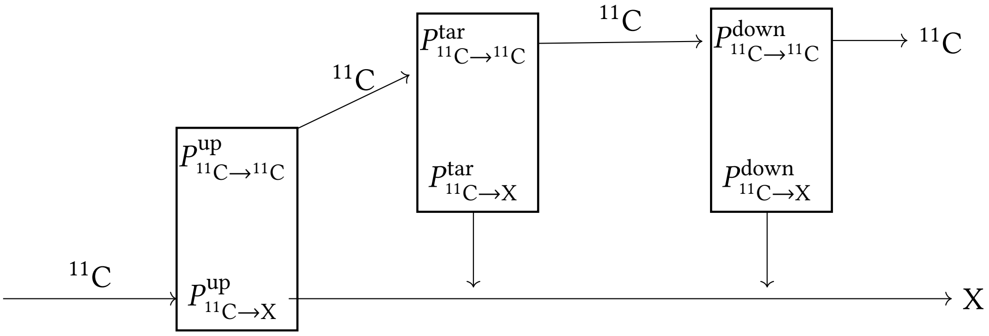

Figure 3.3: Graphical representation of the probability calculations for primary ^{11}C.

3.2.2 Carbon-11 Interactions

To calculate the production probability of ^{11}C in the target, the ^{12}C survival probabilities have to be known. To obtain them an auxiliary measurement with primary ^{11}C is required. The calculation for ^{11}C is much simpler since there are only two signals. An overview of the probabilities can be seen in Fig. 3.3.

Calculation with Target

With the same method as before, the survival probability of ^{11}C can be read as

$$P^{\mathrm{in}}_{^{11}\mathrm{C}\to^{11}\mathrm{C}} = P^{\mathrm{up}}_{^{11}\mathrm{C}\to^{11}\mathrm{C}}\,P^{\mathrm{tar}}_{^{11}\mathrm{C}\to^{11}\mathrm{C}}\,P^{\mathrm{down}}_{^{11}\mathrm{C}\to^{11}\mathrm{C}}. \tag{3.15}$$

by tracing the path of ^{11}C in the diagram. The destruction probability is

$$P^{\mathrm{in}}_{^{11}\mathrm{C}\to\mathrm{X}} = P^{\mathrm{up}}_{^{11}\mathrm{C}\to\mathrm{X}} + P^{\mathrm{up}}_{^{11}\mathrm{C}\to^{11}\mathrm{C}}\,P^{\mathrm{tar}}_{^{11}\mathrm{C}\to\mathrm{X}} + P^{\mathrm{up}}_{^{11}\mathrm{C}\to^{11}\mathrm{C}}\,P^{\mathrm{tar}}_{^{11}\mathrm{C}\to^{11}\mathrm{C}}\,P^{\mathrm{down}}_{^{11}\mathrm{C}\to\mathrm{X}}. \tag{3.16}$$

The terms describe upstream destruction, target destruction and downstream destruction.

Calculation without Target

To calculate the probabilities without the target inserted, the target survival probability is set to one as before in the case of ^{12}C.

$$P^{\mathrm{tar,out}}_{^{11}\mathrm{C}\to^{11}\mathrm{C}} = 1. \tag{3.17}$$

Thus Eq. (3.15) changes to

$$P^{\mathrm{out}}_{^{11}\mathrm{C}\to^{11}\mathrm{C}} = P^{\mathrm{up}}_{^{11}\mathrm{C}\to^{11}\mathrm{C}}\,P^{\mathrm{down}}_{^{11}\mathrm{C}\to^{11}\mathrm{C}}. \tag{3.18}$$

and Eq. (3.16) changes to

$$P^{\mathrm{out}}_{^{11}\mathrm{C}\to\mathrm{X}} = P^{\mathrm{up}}_{^{11}\mathrm{C}\to\mathrm{X}} + P^{\mathrm{up}}_{^{11}\mathrm{C}\to^{11}\mathrm{C}}\,P^{\mathrm{down}}_{^{11}\mathrm{C}\to\mathrm{X}}. \tag{3.19}$$

Dividing Eq. (3.15) by Eq. (3.18) yields the target survival probability:

$$\frac{P^{\mathrm{in}}_{^{11}\mathrm{C}\rightarrow{}^{11}\mathrm{C}}}{P^{\mathrm{out}}_{^{11}\mathrm{C}\rightarrow{}^{11}\mathrm{C}}} = P^{\mathrm{tar}}_{^{11}\mathrm{C}\rightarrow{}^{11}\mathrm{C}} \tag{3.20}$$

3.2.3 Number of Constraints and Unknowns

The number of constraints and unknowns can be read directly from Fig. 3.2 and Fig. 3.3. Every box is one constraint and every probability is one unknown. The number of constraints from measurements is the number of signals minus one. This is due to the conservation of probabilities (all outgoing probabilities add up to one). The target-out case adds additional constraints. The constraints from the boxes, i.e. the probability conservation, and from the measurements are listed in the table below.

Isotope	Boxes	Target in	Target out	Sum	Unknowns
^{12}C	5	3	3	11	13
^{11}C	3	1	1	5	6

Since the target survival probability of ^{11}C can be determined with ^{11}C measurements, one unknown can be eliminated in the ^{12}C case. This still leaves one unknown more than there are constraints. In the following, two possibilities to determine the remaining unknown are discussed. The first one eliminates the upstream probabilities and estimates the downstream probabilities. The second one eliminates the downstream probabilities and estimates the upstream probabilities.

Downstream Measurement

Using the detectors inside the magnetic field, it is possible to reconstruct the interaction vertices. Based on them the downstream interactions can be identified. This can be used to measure downstream interactions. It is important to measure the downstream survival probability of all primaries. The production probability in the target can be calculated as

$$P^{\mathrm{tar}}_{^{12}\mathrm{C}\rightarrow{}^{11}\mathrm{C}} = \frac{P^{\mathrm{down}}_{^{12}\mathrm{C}\rightarrow{}^{12}\mathrm{C}}}{P^{\mathrm{down}}_{^{11}\mathrm{C}\rightarrow{}^{11}\mathrm{C}}} \frac{1}{P^{\mathrm{out}}_{^{12}\mathrm{C}\rightarrow{}^{12}\mathrm{C}}} \left(P^{\mathrm{in}}_{^{12}\mathrm{C}\rightarrow{}^{11}\mathrm{C}} - P^{\mathrm{out}}_{^{12}\mathrm{C}\rightarrow{}^{11}\mathrm{C}} \frac{P^{\mathrm{in}}_{^{11}\mathrm{C}\rightarrow{}^{11}\mathrm{C}}}{P^{\mathrm{out}}_{^{11}\mathrm{C}\rightarrow{}^{11}\mathrm{C}}} \right). \tag{3.21}$$

The downstream probabilities are smaller than the upstream probabilities and the measurements are expected to have higher uncertainties. Thus this method is not recommended.

Upstream Calculation

Since the detectors upstream are known, the upstream probabilities can be estimated. The probability for ^{11}C production is difficult to calculate. However, calculating the ^{12}C and ^{11}C survival probabilities is feasible.

The detector with the most material is a plastic scintillator [10, Tab. 1]. According to the scintillator data sheet [18], it consists of polyvinyl toluene. This is a polymer with an H-to-C ratio of 1.104. Its interaction lengths can be calculated from the measured total cross sections. This calculation requires only the target survival probabilities. Thus it can be done before calculating the production probability.

The production probability in the target can be calculated as

$$P^{\mathrm{tar}}_{^{12}\mathrm{C}\to{}^{11}\mathrm{C}} = \frac{P^{\mathrm{up}}_{^{11}\mathrm{C}\to{}^{11}\mathrm{C}}}{P^{\mathrm{up}}_{^{12}\mathrm{C}\to{}^{12}\mathrm{C}}} \frac{1}{P^{\mathrm{out}}_{^{11}\mathrm{C}\to{}^{11}\mathrm{C}}} \left(P^{\mathrm{in}}_{^{12}\mathrm{C}\to{}^{11}\mathrm{C}} - P^{\mathrm{out}}_{^{12}\mathrm{C}\to{}^{11}\mathrm{C}} \frac{P^{\mathrm{in}}_{^{11}\mathrm{C}\to{}^{11}\mathrm{C}}}{P^{\mathrm{out}}_{^{11}\mathrm{C}\to{}^{11}\mathrm{C}}} \right). \tag{3.22}$$

This calculation introduces a systematic uncertainty due to the neglect of other upstream detectors. Note that the upstream material budget only enters as a ratio of ^{12}C and ^{11}C survival probabilities. This is a factor close to one for which the exact upstream material budget cancels out. In the previous analysis, a numerical approximation to marginalize over several unknown quantities was used [12]. This resulted in a relative systematic uncertainty of 3% which is eliminated by the method proposed in this section. The remaining systematic uncertainty is considered to be negligible in the latest release of results from the 2018 pilot run [14].

3.3 Boron Production Probabilities

For the astrophysically important production of boron from carbon, both stable isotopes ^{11}B and ^{10}B have to be considered. The production of ^{11}B from ^{12}C can be calculated similar to the production of ^{11}C from ^{12}C as described in Section 3.2. The $^{11}\mathrm{B}^{\mathrm{down}}$ signal can be identified by a charge change inside the detector. With primary ^{11}B measurements similar to Fig. 3.3 can be done. The survival probability in the target $P^{\mathrm{tar}}_{^{11}\mathrm{B}\to{}^{11}\mathrm{B}}$ and the production probability $P^{\mathrm{tar}}_{^{12}\mathrm{C}\to{}^{11}\mathrm{B}}$ can be calculated this way.

The ^{10}B production from ^{12}C requires additional steps which are described in Section 3.3.1. They are necessary since ^{10}B can be produced from ^{11}B and ^{11}C as well. Measurements with ^{10}B produced from primary ^{11}C or ^{11}B can be done similar to Fig. 3.2. For this to yield usable results, measurements with primary ^{10}B similar to Fig. 3.3 are required as well. The following probabilities are obtained from these measurements:

$$P^{\mathrm{tar}}_{^{11}\mathrm{C}\to{}^{10}\mathrm{B}} \qquad P^{\mathrm{tar}}_{^{11}\mathrm{B}\to{}^{10}\mathrm{B}} \qquad P^{\mathrm{tar}}_{^{10}\mathrm{B}\to{}^{10}\mathrm{B}} \tag{3.23}$$

3.3.1 Boron-10 Interactions

The ^{10}B production from ^{12}C can be measured according to Fig. 3.4.

The $^{10}\mathrm{B}^{\mathrm{down}}_{^{12}\mathrm{C}}$ signal can be identified by a charge change without a rigidity change. The $^{10}\mathrm{B}^{\mathrm{down}}_{^{11}\mathrm{C}}$ signal can be identified by a charge and a rigidity change. The $^{10}\mathrm{B}^{\mathrm{down}}_{^{11}\mathrm{B}}$ signal can be identified by a rigidity change without a charge change. If those three signals can be reliably separated from the ^{10}B signal, it is possible to treat them as X and eliminate their production probabilities. In this case the ^{10}B production probability is

$$\begin{aligned}
P^{\mathrm{in}}_{^{12}\mathrm{C}\to{}^{10}\mathrm{B}} = {} & P^{\mathrm{up}}_{^{12}\mathrm{C}\to{}^{10}\mathrm{B}}\, P^{\mathrm{tar}}_{^{10}\mathrm{B}\to{}^{10}\mathrm{B}}\, P^{\mathrm{down}}_{^{10}\mathrm{B}\to{}^{10}\mathrm{B}} \\
& + P^{\mathrm{up}}_{^{12}\mathrm{C}\to{}^{11}\mathrm{B}}\, P^{\mathrm{tar}}_{^{11}\mathrm{B}\to{}^{10}\mathrm{B}}\, P^{\mathrm{down}}_{^{10}\mathrm{B}\to{}^{10}\mathrm{B}} \\
& + P^{\mathrm{up}}_{^{12}\mathrm{C}\to{}^{11}\mathrm{C}}\, P^{\mathrm{tar}}_{^{11}\mathrm{C}\to{}^{10}\mathrm{B}}\, P^{\mathrm{down}}_{^{10}\mathrm{B}\to{}^{10}\mathrm{B}} \\
& + P^{\mathrm{up}}_{^{12}\mathrm{C}\to{}^{12}\mathrm{C}}\, P^{\mathrm{tar}}_{^{12}\mathrm{C}\to{}^{10}\mathrm{B}}\, P^{\mathrm{down}}_{^{10}\mathrm{B}\to{}^{10}\mathrm{B}}
\end{aligned} \tag{3.24}$$

The first term describes upstream ^{10}B production. The following terms describe ^{10}B production from ^{11}B, ^{11}C and ^{12}C respectively.

With the same considerations as in Section 3.2, the number of constraints and unknowns can be obtained. Figure 3.4 contains 31 unknowns, 9 boxes and 9 signals. Target-out measurements yield 9 additional signals. There are a total of 27 constraints. Three of the remaining four unknowns come from other measurements. Again the last remaining unknown has to be estimated by calculating the ratio of upstream probabilities.

The production probability for ^{10}B from ^{12}C inside the target is

$$\begin{aligned}
P^{\mathrm{tar}}_{^{12}\mathrm{C}\to{}^{10}\mathrm{B}} = {} & \frac{P^{\mathrm{up}}_{^{10}\mathrm{B}\to{}^{10}\mathrm{B}}}{P^{\mathrm{up}}_{^{12}\mathrm{C}\to{}^{12}\mathrm{C}}} \frac{1}{P^{\mathrm{out}}_{^{10}\mathrm{B}\to{}^{10}\mathrm{B}}} \\
& \Bigg[P^{\mathrm{in}}_{^{12}\mathrm{C}\to{}^{10}\mathrm{B}} \\
& \quad - \frac{P^{\mathrm{in}}_{^{11}\mathrm{B}\to{}^{10}\mathrm{B}}\, P^{\mathrm{out}}_{^{12}\mathrm{C}\to{}^{11}\mathrm{B}}}{P^{\mathrm{out}}_{^{11}\mathrm{B}\to{}^{11}\mathrm{B}}} - \frac{P^{\mathrm{in}}_{^{11}\mathrm{C}\to{}^{10}\mathrm{B}}\, P^{\mathrm{out}}_{^{12}\mathrm{C}\to{}^{11}\mathrm{C}}}{P^{\mathrm{out}}_{^{11}\mathrm{C}\to{}^{11}\mathrm{C}}} \\
& - \frac{P^{\mathrm{in}}_{^{10}\mathrm{B}\to{}^{10}\mathrm{B}}}{P^{\mathrm{out}}_{^{10}\mathrm{B}\to{}^{10}\mathrm{B}}} \Bigg(P^{\mathrm{out}}_{^{12}\mathrm{C}\to{}^{10}\mathrm{B}} \\
& \quad - \frac{P^{\mathrm{out}}_{^{11}\mathrm{B}\to{}^{10}\mathrm{B}}\, P^{\mathrm{out}}_{^{12}\mathrm{C}\to{}^{11}\mathrm{B}}}{P^{\mathrm{out}}_{^{11}\mathrm{B}\to{}^{11}\mathrm{B}}} - \frac{P^{\mathrm{out}}_{^{11}\mathrm{C}\to{}^{10}\mathrm{B}}\, P^{\mathrm{out}}_{^{12}\mathrm{C}\to{}^{11}\mathrm{C}}}{P^{\mathrm{out}}_{^{11}\mathrm{C}\to{}^{11}\mathrm{C}}} \Bigg) \Bigg]
\end{aligned} \tag{3.25}$$

This equation is similar to Eq. (3.22) with additional terms to correct for ^{10}B production from other isotopes. The upstream survival probabilities can be calculated from the target survival probabilities as in the ^{11}C case.

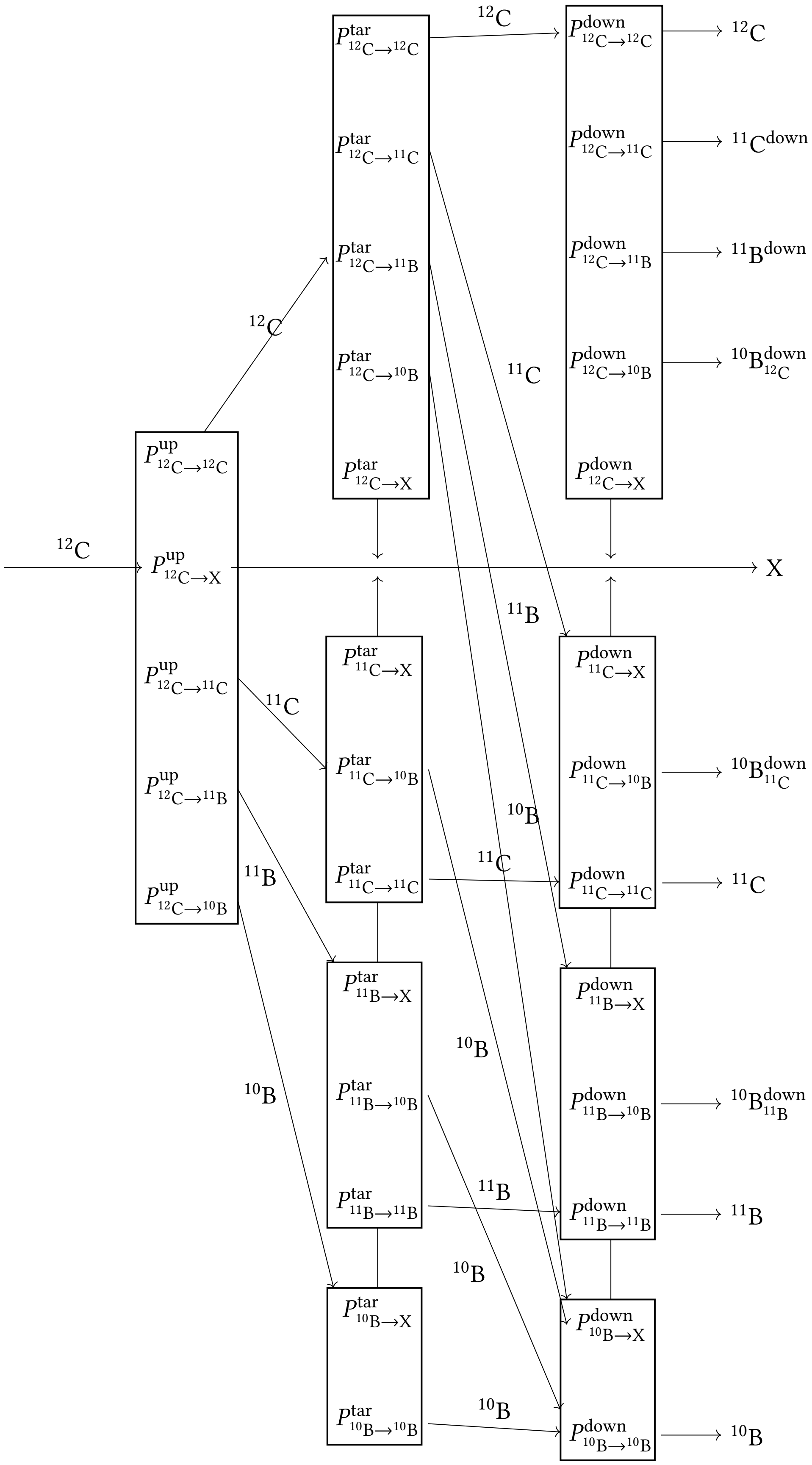

Figure 3.4: Graphical representation of the probability calculations for the production of Carbon-11, Boron-11 and Boron-10 from primary Carbon-12.

3.3.2 Outlook: Beryllium and Lithium

The presented calculations for boron are already in use for the analysis of the pilot run [14]. For future measurements, the calculations have to be extended to beryllium and lithium. To ease the process, drawing the diagrams could be automated. Solving the equations obtained from the diagrams by hand is tedious. For the ^{10}B calculations the equations were solved by a computer algebra system. These systems provide an option to convert formulas into executable code. This can be used to seamlessly integrate even more complex results into the analysis. Therefore the developed method is considered to be applicable for the beryllium and lithium production as well.

3.4 Analytical Description of the Target

In [12] it was suggested to use a thin target for the measurement. During the 2018 measurements, a 1.5 cm polyethylene and a 1.0 cm carbon target were used. The general idea of using a thin target is, that only the first interaction in the target is of interest. All subsequent interactions are unwanted and add uncertainty to the measurement. In the target, a primary nucleus, i.e. a beam particle, can interact with the target material and fragment into a secondary nucleus. The secondary nucleus can interact again and fragment into a tertiary nucleus and so on. Interactions of secondary nuclei remove them from the downstream measurement. In addition, they can add to the measurements of other nuclei. This process is called feed-down. To prevent both the disappearance of secondary nuclei and feed-down, a thin target is chosen to reduce the amount of secondary interactions. The disadvantage of using a thin target is the reduction of primary interactions. Most particles will pass through a thin target without interacting, so only a small number of interactions can be observed.

Instead of using a thin target to reduce the effects of destruction and feed-down, measuring these effects with additional primaries is possible. This will not only enable us to use a thicker target, but it will also help to reduce uncertainties. Even in the thin target case, the number of destroyed and feed-down particles has to be quantified. A full analytical description of the processes inside the target is required for this. This section derives and discusses such a description.

The following calculations use interaction lengths to describe the properties of the target. An interaction length is a material constant that depends on the density and composition of the target. Given the number density n_C of atoms in the carbon target, the interaction length for a process $i \longrightarrow j$ is

$$\lambda^\mathrm{C}_{i\rightarrow j} = \frac{1}{n_\mathrm{C}\,\sigma_{\mathrm{C},i\rightarrow j}} \tag{3.26}$$

where $\sigma_{\mathrm{C},i\rightarrow j}$ is the cross section of an isotope i fragmenting into j on a carbon nucleus. In the polyethylene target, n_PE is the number of $\mathrm{CH_2}$ units per volume. Thus the interaction length is

$$\lambda^{\mathrm{PE}}_{i\to j} = \frac{1}{n_{\mathrm{PE}}\,\sigma_{\mathrm{C},i\to j} + 2n_{\mathrm{PE}}\,\sigma_{\mathrm{H},i\to j}} \tag{3.27}$$

with the hydrogen cross section $\sigma_{\mathrm{H},i\to j}$. By measuring both interaction lengths, the hydrogen cross section can be calculated as

$$\sigma_{\mathrm{H},i\to j} = \frac{1}{2}\left(\frac{1}{n_{\mathrm{PE}}\,\lambda^{\mathrm{PE}}_{i\to j}} - \frac{1}{n_{\mathrm{C}}\,\lambda^{\mathrm{C}}_{i\to j}}\right). \tag{3.28}$$

This corresponds to the subtraction of the carbon cross section from the polyethylene cross section.

3.4.1 Analytical Description

To fully understand what is happening inside the target, an analytical description is needed. Let x be the distance traveled through the target and λ_i the interaction length of an isotope i. The number $N_i(x)$ of nuclei present at any position x is

$$N_i(x) = N_i(0)\exp\left(-\frac{x}{\lambda_i}\right). \tag{3.29}$$

This follows from the simple consideration that the number $-dN_i$ of particles destroyed in each interval dx is

$$\frac{dN_i}{dx} = -\frac{1}{\lambda_i}N_i. \tag{3.30}$$

When a nucleus of type i fragments into a nucleus of type j with an interaction length $\lambda_{i\to j}$, the production of nuclei from type j is

$$\frac{dN_j}{dx} = \frac{1}{\lambda_{i\to j}}N_i. \tag{3.31}$$

Combining this with the destruction of particles the differential equation for N_j is

$$\frac{dN_j}{dx} = \frac{1}{\lambda_{i\to j}}N_i - \frac{1}{\lambda_j}N_j. \tag{3.32}$$

To describe feed-down a third isotope k can be introduced that can be produced by fragmenting both other isotopes,

$$\frac{dN_k}{dx} = \frac{1}{\lambda_{i\to k}}N_i + \frac{1}{\lambda_{j\to k}}N_j - \frac{1}{\lambda_k}N_k. \tag{3.33}$$

Since lighter isotopes can never fragment into heavier ones, N_i and N_j are independent of N_k. This allows solving the differential equations of heavier isotopes first and plugging their solutions into the light isotope equations. To make it easier to write down the solution, a matrix M is introduced [19],

$$M_{ij} = \begin{cases} \frac{1}{\lambda_{j \to i}} & \text{if } j \text{ fragments to } i, \\ -\frac{1}{\lambda_i} & \text{if } i = j, \\ 0 & \text{otherwise.} \end{cases} \tag{3.34}$$

The system of differential equations can now be written as

$$\frac{d}{dx}\vec{N}(x) = M\,\vec{N}(x) \tag{3.35}$$

where $\vec{N}(x) = (N_1(x), \ldots, N_n(x))^{\mathrm{T}}$ is a vector of particle numbers. The solution is

$$\vec{N}(x) = \exp(Mx)\,\vec{N}(0). \tag{3.36}$$

The exponential function is to be understood as a matrix exponential,

$$\exp(Mx) = I + Mx + \frac{1}{2}(Mx)^2 + \cdots . \tag{3.37}$$

For thin targets, x is considered to be small. Thus higher orders do not contribute and a linear approximation can be done,

$$N_i(x) \approx N_i(0) + \sum_j M_{ij}\,N_j(0)\,x + O(x^2). \tag{3.38}$$

Exact solutions can be calculated by diagonalizing M. When the isotopes are ordered by their mass from heaviest to lightest, M is a triangular matrix and thus its eigenvalues are the elements on the diagonal. Given an eigenbasis V the matrix exponential is

$$\exp(Mx) = V\,\mathrm{diag}\left(\exp(M_{11}x), \ldots, \exp(M_{nn}x)\right)\,V^{-1}. \tag{3.39}$$

The eigenbasis V is independent of x and defined by

$$M = V\,\mathrm{diag}\left(M_{11}, \ldots, M_{nn}\right)\,V^{-1}. \tag{3.40}$$

Finding solutions for an arbitrary number of isotopes is reduced to a linear algebra problem. This makes it possible to find all analytical solutions with a computer algebra system in a reasonable time.

3.4.2 Calculation of Interaction Lengths

If the number of incoming and outgoing particles is known, the equations can be solved for the matrix elements. In the following equations, a pure beam is assumed, i.e. $N_i(0) \neq 0$ for exactly one isotope. The matrix element for the primary isotope is

$$-\frac{1}{\lambda_i} = M_{ii} = \frac{1}{x}\ln\frac{N_i(x)}{N_i(0)}. \tag{3.41}$$

For secondary isotopes, the off-diagonal matrix elements are

$$\frac{1}{\lambda_{i\to j}} = M_{ji} = \frac{M_{jj} - M_{ii}}{\exp(M_{jj}x) - \exp(M_{ii}x)} \frac{N_j(x)}{N_i(0)}. \tag{3.42}$$

In this equation M_{jj} appears. To solve for M_{jj} an auxiliary measurement with $N_j^{(j)}(0) \neq 0$ is needed. In this case the solution for M_{ji} is

$$\frac{1}{\lambda_{i\to j}} = M_{ji} = \frac{1}{x} \frac{N_j^{(j)}(0)\, N_j(x)}{N_i(0)\, N_j^{(j)}(x) - N_j^{(j)}(0)\, N_i(x)} \left(\ln \frac{N_j^{(j)}(x)}{N_j^{(j)}(0)} - \ln \frac{N_i(x)}{N_i(0)} \right). \tag{3.43}$$

For each secondary isotope, an auxiliary measurement is needed. The factor in Eq. (3.42) in linear approximation is

$$\frac{M_{jj} - M_{ii}}{\exp(M_{jj}\, x) - \exp(M_{ii}\, x)} \approx \frac{M_{jj} - M_{ii}}{M_{jj}\, x - M_{ii}\, x + O(x^2)} = \frac{1}{x} \tag{3.44}$$

which results in an interaction length

$$\lambda_{i\to j} = x\, \frac{N_i(0)}{N_j(x)} \tag{3.45}$$

as expected. For secondary isotopes auxiliary measurements are not needed in linear approximation.

For matrix elements featuring isotopes that can be produced from secondaries, additional feed-down terms are required. A matrix element M_{ki} contains contributions from M_{ji}, M_{kj} and all three diagonal elements. An explicit discussion of those terms is omitted since no new insights are gained from their analytical structure.

Figure 3.5 shows a comparison between the linear approximation and the exact solution with and without feed-down. The destruction interaction lengths of 25 cm for the primary and 15 cm for the secondary particles are arbitrary but in the same order of magnitude as for carbon primaries. The production lengths of 30 cm each are chosen to be unrealistically low for illustrative purposes.

3.4.3 Uncertainties

The uncertainty on the measurement of a matrix element M_{ij} is

$$\Delta M_{ij}^2 = \sum_{k,l} \left(\frac{dM_{ij}}{dN_k^{(l)}(x)} \Delta N_k^{(l)}(x) \right)^2 . \tag{3.46}$$

It can be calculated by expressing the matrix element as a function of the particle numbers.

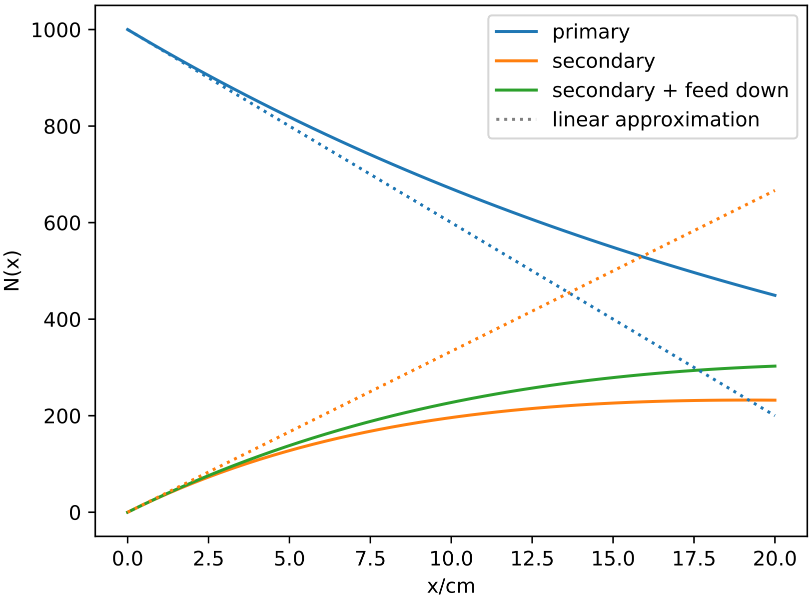

Figure 3.5: Comparison between exact solution (solid lines) and linear approximation (dotted lines) for primary and secondary particles. Additionally, the effect of feed-down is shown. The total interaction lengths are 25 cm for the primary and 15 cm for the secondary particles. The production lengths are 30 cm each.

The uncertainties on the particle numbers are assumed to be Poissonian,

$$\Delta N_k^{(l)}(x) = \sqrt{N_k^{(l)}(x)}. \tag{3.47}$$

To find the optimal target thickness, the minimum of Eq. (3.46) has to be found. Typically there is no analytical solution for most matrix elements and numerical methods are required. How to explicitly calculate the uncertainties is discussed in Section 3.5.5.

This method gives mathematically rigorous treatment to the interaction length and uncertainty calculation. In contrast to the previous analysis [12, 13] where destruction and feed-down were treated as corrections. These corrections introduced a large – e.g. about 3% for the ^{11}C production cross section – systematic uncertainty. The uncertainties provided in Eq. (3.46) depend on the statistical uncertainties of the measurements. Thus they automatically decrease with higher statistics.

3.5 Target Thickness Optimization

To find the optimal target thickness for a particular experiment, a number of software tools have been developed. To obtain the required numbers of incoming particles and interaction lengths, beam and target simulations are analyzed. All analytical calculations

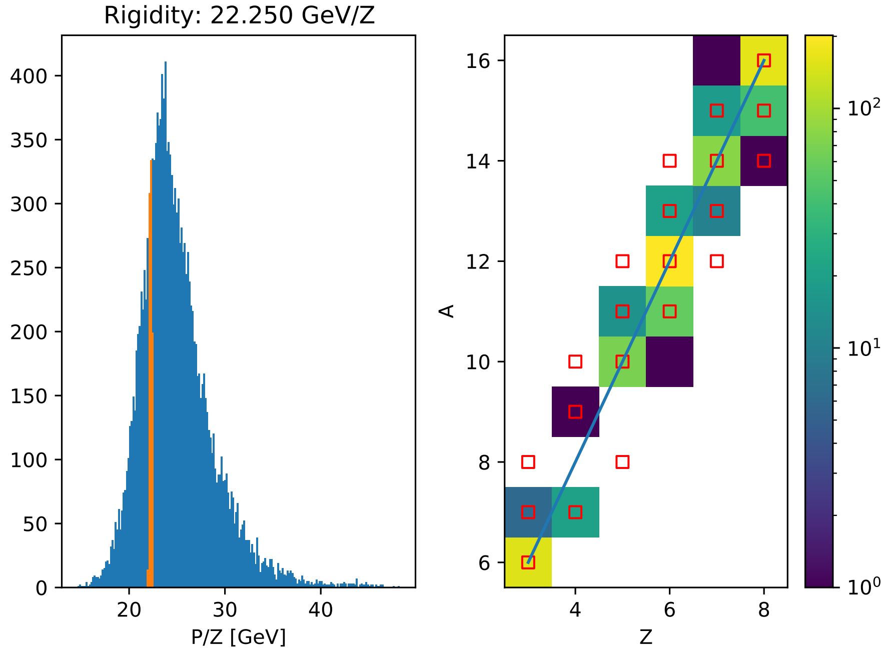

Figure 3.6: An example rigidity cut. The left side shows the rigidity distribution of all beam particles and the selected rigidity cut. In this case, the cut is at 22.25 GeV per charged nucleon with a width of 1%. The right side shows the distribution of nuclei with specific charge and mass numbers passing the cut. The red boxes mark the nuclei produced inside the target in case of an oxygen beam.

are done with a Mathematica notebook [20]. Finally, the analytical expressions for the uncertainties are evaluated with the simulated numbers as input.

3.5.1 Beam Simulation

To get the number of incoming particles, i.e. the beam particles, for each isotope, beam simulations are analyzed. The beam particles are from FLUKA [21] simulations of ^{207}Pb on 300 mm Be from [22]. The particles are created by fragmenting lead ions on a beryllium block. A rigidity selection is performed afterward. The width of the accepted rigidity interval and its center position are free parameters. For further analysis, a cut with a reasonable amount of all required isotopes should be selected. Figure 3.6 shows the process of finding a good rigidity cut. The width of the cut is limited to about 1% of the rigidity since the isotope identification depends on a well-known rigidity. For 22.25 GeV per charged nucleon, the highest number of required isotopes is present in the beam. The following analysis uses this cut.

If not all isotopes appearing in the interaction matrix are present in the beam, their interaction lengths must be supplied in other ways. Using interaction lengths from model predictions instead of measurements introduces uncertainties that are difficult to quantify.

Therefore, it should always be preferred to measure all interaction lengths with the respective primaries. However, based on the beam simulations this can not be achieved by any rigidity cut.

3.5.2 Target Simulation

The SHINE Offline Framework [23] is used to generate target simulations [24]. Here a pure oxygen beam and two 50 cm targets – a polyethylene and a carbon target – are used. In the pilot run ^{12}C cross sections were measured whereas in future measurements cross sections of heavier elements should be measured. The vertices where nuclei fragment into lower mass nuclei are extracted from the simulation and their position is recorded. Additionally, the parent and daughter nuclei of each fragmentation are counted. Based on this, two methods can be used to extract the interaction lengths.

3.5.3 Full Target Model Fitting

Since the positions of the production and destruction vertices of each nucleus are known in the simulation, it is possible to calculate the number $N_i(x)$ of nuclei present at every position x in the target. This allows fitting the model described in Section 3.4.1 to the acquired $N_i(x)$ and obtaining the interaction matrix. The fit is performed for one isotope at a time, starting with the heaviest isotope. Matrix elements obtained from heavier isotopes are used as constants in the fits for lighter isotopes. In Fig. 3.7 example fits are shown labeled as (1).

While this method fits the simulation perfectly, it is prone to overfitting. Errors from heavy isotopes can propagate to lighter isotopes and get compensated by introducing new errors.

3.5.4 Use of Branching Ratios

By simply counting interactions, the branching ratios for all interactions can be calculated. The branching ratio $B_{j\to i}$ of an interaction $j \to i$ is the number of particles i produced from particle j divided by the total number of interactions fragmenting j. Knowing the branching ratios, the matrix elements can be calculated by multiplying the branching ratios by the total interaction rate of the parent nucleus as

$$M_{ij} = -M_{jj}\, B_{j\to i}. \tag{3.48}$$

The total interaction length can be calculated by fitting an exponential function to the distribution of travel distances for each isotope. In Fig. 3.7 plots of the target model with the matrix obtained from branching ratios are shown labeled as (2). The obtained matrix describes all isotopes well, except ^{6}Li. This is due to a systematic underestimation of the ^{6}Li production.

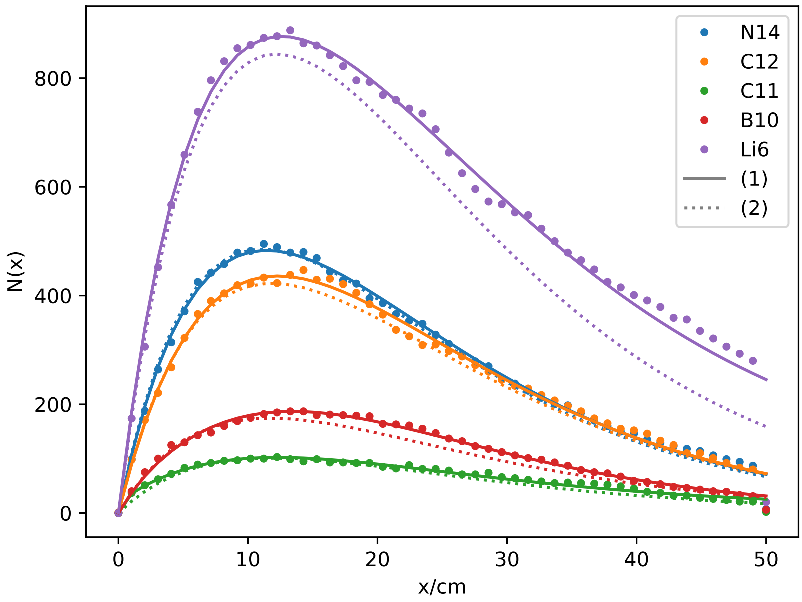

Figure 3.7: Simulated particle counts $N_i(x)$ of prominent isotopes. The beam consists of $5 \cdot 10^4$ ^{16}O particles which are not shown in the figure. ^{14}N and ^{12}C are common particles produced from ^{16}O. ^{6}Li is the main feed-down particle for oxygen interactions. Additionally, data points for the astrophysically important particles ^{11}C and ^{10}B are shown. The two fitting methods shown as (1) and (2) are described in the text.

While this method provides independent results, it requires high statistics. To achieve high statistics, simulations with many beam particles are required ($N > 10^5$). The required number of beam particles was reduced by using different beam particles.

A visualization of the resulting matrix elements is shown in Fig. 3.8 for a carbon target. Dark red squares indicate high interaction rates. These can be seen especially for ^{12}C and ^{6}Li, which are subject to heavy feed-down. For example ^{14}N, which is a common product from ^{16}O fragmentation, fragments further down to ^{12}C.

3.5.5 Uncertainty Calculation

The uncertainties on the interaction length measurements are calculated with a Mathematica notebook. The following enumeration describes the functionality of the notebook:

1. Data from simulation analysis is read and required isotopes are defined.
2. The matrix is defined and the matrix exponential is calculated.
   This step is computationally demanding since an analytical eigenbasis for the matrix has to be found.

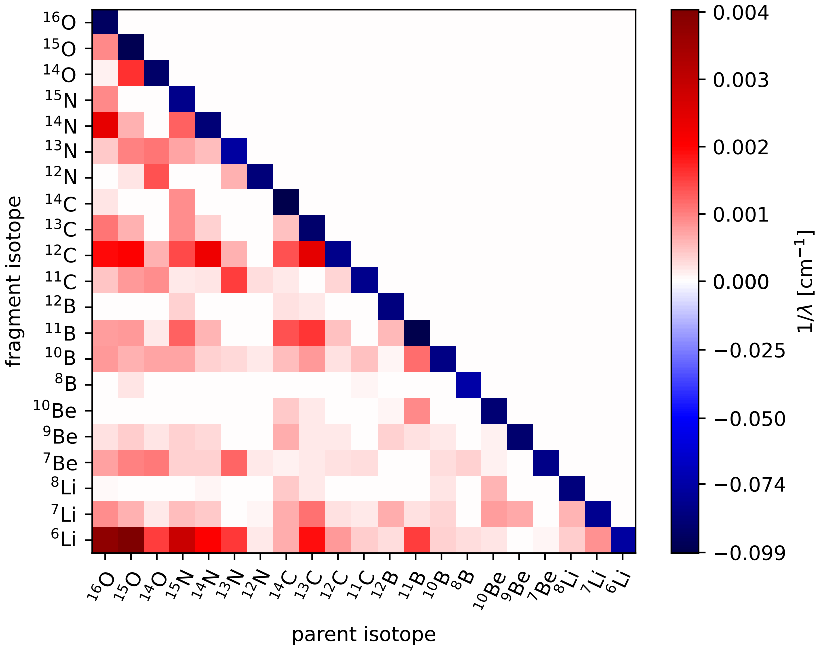

Figure 3.8: Visual representation of the interaction matrix. The negative destruction rates are on the diagonal. They are the inverse of the total interaction lengths. In the lower-left half are the production rates. Their inverse is the partial interaction length.

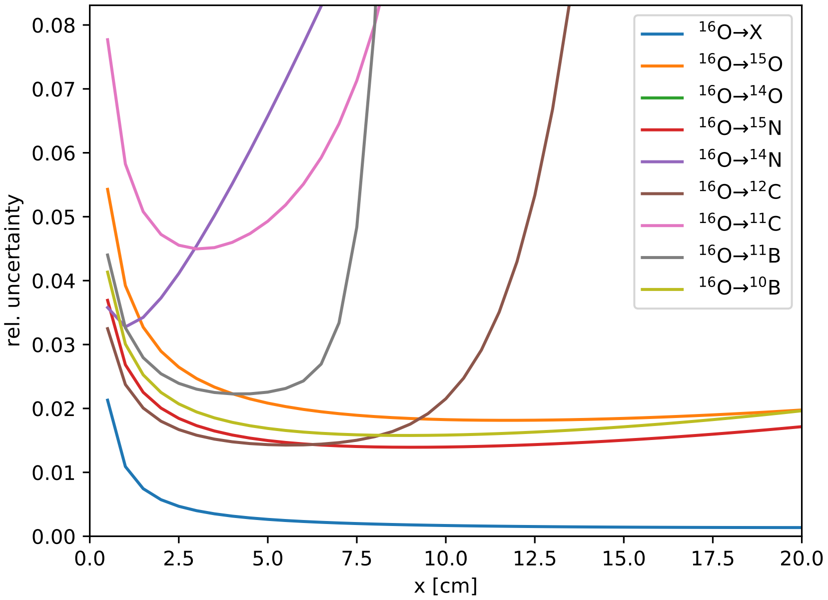

Figure 3.9: Relative uncertainties on the interaction rates of all ^{16}O interactions down to boron in the carbon target.

3. The matrix equation is defined and solved for all isotopes.
4. The solutions are recursively inserted into each other until all matrix elements vanish.
   After this step, the solutions only depend on measurements.
5. The uncertainties are calculated according to Eq. (3.46).
6. Outgoing particle numbers are calculated with the numerical values for the matrix elements.
7. All numerical values are inserted into the uncertainty functions.
8. The uncertainties are plotted and written to a file.
   Based on this output uncertainties can be numerically minimized by other programs.
9. Optionally the minima are calculated with semi-analytical methods.

All intermediate results are stored. The plots are later superimposed as shown in Fig. 3.9. Most uncertainties have a common interval in which they are reasonably low. The optimal target thickness is in this interval. The specific value depends on the priority of the interaction rates to be measured. Astrophysically important interaction rates should have a lower uncertainty.

For example, the optimal uncertainty for the boron production from oxygen can be achieved with a 3 cm carbon target. Such a target would have the lowest uncertainty for ^{11}C (decays into ^{11}B), ^{11}B and ^{10}B. The 1 cm target used in the pilot run would yield a 40% higher uncertainty. This indicates that a significant reduction of uncertainties could be achieved with a thicker target.

4 Neutral Pion Production in Pion-Carbon Interactions

In 2009, NA61 took data for π^--C interactions. The data was analyzed for charged hadrons and weakly decaying particles [11]. The results are crucial for the understanding of hadronic showers. However, the data was not analyzed for electromagnetic decays of neutral hadrons. Since NA61 is a hadron spectrometer, this is not surprising. NA61 can not detect photons. In this chapter, it will be shown that measurements of photon and neutral pion spectra with NA61 are feasible nonetheless.

The importance of such measurements is evident: Photons are produced in the decay of neutral pions that are produced in pion-nucleus interactions. The photon yield thus allows us to calculate the π^0 production. Additionally, measuring the photon spectrum sets an upper bound to the energy available for hadron production. The energy of the electromagnetic shower can be measured directly and thus the energy loss of the hadronic shower. As discussed in Section 1.2, this also limits the muon number observed in extensive air showers.

The key idea of the analysis is to reconstruct photons from the electron-positron pairs they produce. Pair production happens inside the target – in this case, a graphite block – and converts a fraction of the photons into e^+e^- pairs. Since electrons are charged particles, they can be detected by NA61. They can be identified by their energy loss in the TPCs as described in Section 4.4. When a pair of particles is found by NA61, it is necessary to ensure that it is an actual e^+e^- pair from pair production. This can be done by calculating the invariant mass of the pair as explained in Section 4.5. Just like every other experiment, NA61 is not a perfect detector. Thus several corrections have to be applied to get the final result. These corrections are discussed in Section 4.6. The result is shown in Section 4.7.

Before the analysis can start, a set of preliminary considerations is required. The pair production mechanism is discussed in Section 4.1. This includes the kinematics of the electron-positron pair and the cross section calculation. Photons are produced not only by neutral pion decays but by other meson decays as well. These decays produce additional e^+e^- pairs which have to be considered as well. The sources of e^+e^- pairs and how their spectra are related to the pair spectrum are discussed in Section 4.2. How the data for the analysis was obtained and reconstructed is described in Section 4.3.

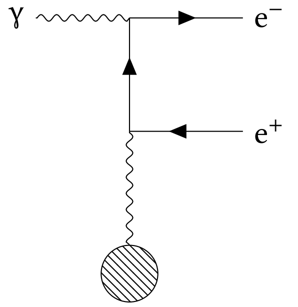

Figure 4.1: Diagram of a photon producing an electron-positron pair. A part of the photon momentum is transferred to a nucleus.

4.1 Pair Production

Photons convert into electron-positron pairs in the target. To produce an electron-positron pair, the photon has to transfer a part of its momentum to a nucleus. This is illustrated in Fig. 4.1. The momentum transfer is small, but it affects the kinematics of the pair production. The kinematics is discussed in Section 4.1.1. Not all photons produce electron-positron pairs in the target. The pair production probability in the target can be calculated from the production cross section. This is explained in Section 4.1.2.

4.1.1 Pair Kinematics

Calculating the kinematics of a decay is simple. In the rest frame of the decaying particle, the produced particles are emitted in opposite directions. Boosting back into the lab frame yields the spectra of the produced pair. Photons do not have a rest frame and thus can not decay. Pair production can only happen in the electric field of a nucleus. The combined system of photon and nucleus does have a well-defined center-of-momentum frame. Since the electron-positron pair is produced in an electric field, its kinematics is nevertheless nontrivial. Many quantum mechanical calculations were done to tackle the problem of pair production. A summary of these calculations and their results can be found in [25]. This section will discuss a few of those formulas that are useful for interpreting the results of the pair analysis.

The most important thing to note is that the photon can not transfer its entire energy to the produced e^+e^- pair. A part of its energy is transferred to the nucleus, resulting in a nuclear recoil. The minimum energy transferred is

$$q_{\min} = k - \sqrt{k^2 - 4m_e^2} \tag{4.1}$$

where k is the photon energy and m_e is the electron mass in natural units. In the high energy limit $k \gg m_e$ this results in a $q_{\min} \propto 1/k$ dependency. The maximum energy transferred is

$$q_{\max} = \frac{k(k+M)}{2k+M}. \tag{4.2}$$

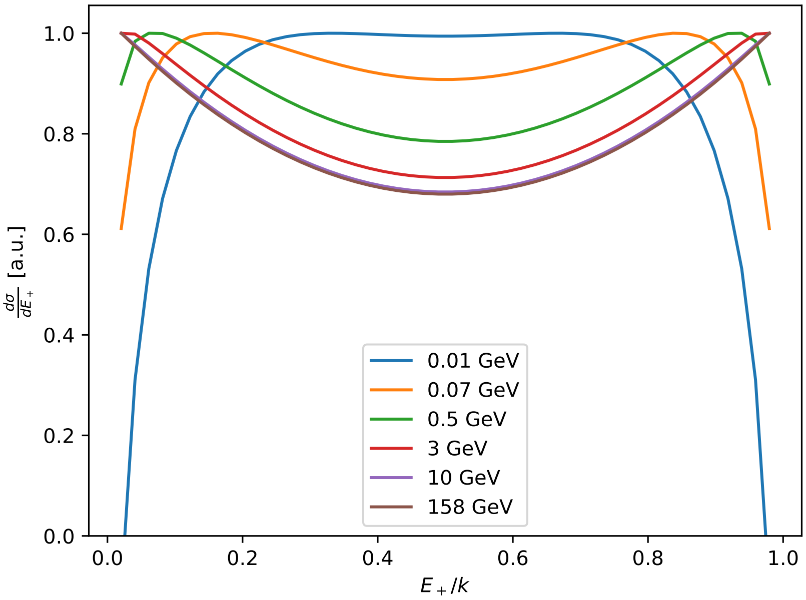

Figure 4.2: Visualization of Eq. (4.3) as a function of energy transferred to the positron. The cross sections are scaled to a common maximum for better comparability.

It depends on the mass M of the nucleus. While $q_{\max}/k$ shrinks with higher photon energies, it does not approach zero. Simulations suggest that high momentum transfer is suppressed in the energy range of interest.

A much more important effect is the distribution of energy between the electron and positron. The energy fraction transferred to the electron and positron for different photon energies is shown in Fig. 4.3. It closely follows the shape of the differential cross section depending on the positron energy,

$$\frac{d\sigma}{dE_+} = \frac{\alpha Z^2 r_0^2}{k^3} \left(\left(E_+^2 + E_-^2\right) \left(\Phi_1(\gamma) - \frac{4}{3} \ln Z\right) + \frac{2}{3} E_+ E_- \left(\Phi_2(\gamma) - \frac{4}{3} \ln Z\right) \right). \tag{4.3}$$

The equation is visualized in Fig. 4.2. Positron energy E_+ and electron energy E_- can be swapped to get the cross section for electrons. Note that $E_\pm \approx p_\pm$ in natural units for high energies. The constants are the fine-structure constant α, the classical electron radius r_0 and the charge number Z of the nucleus. The screening functions $\Phi_{1/2}(\gamma)$ contain corrections for low electron and positron energies. Screening describes the reduction of the effective charge of the nucleus by surrounding electrons. It depends on the screening parameter $\gamma \propto k/(E_+ E_-)$ which is large if either the electron or positron energy is low. Large screening reduces the cross section. For high electron and positron energies, the screening functions are constant.

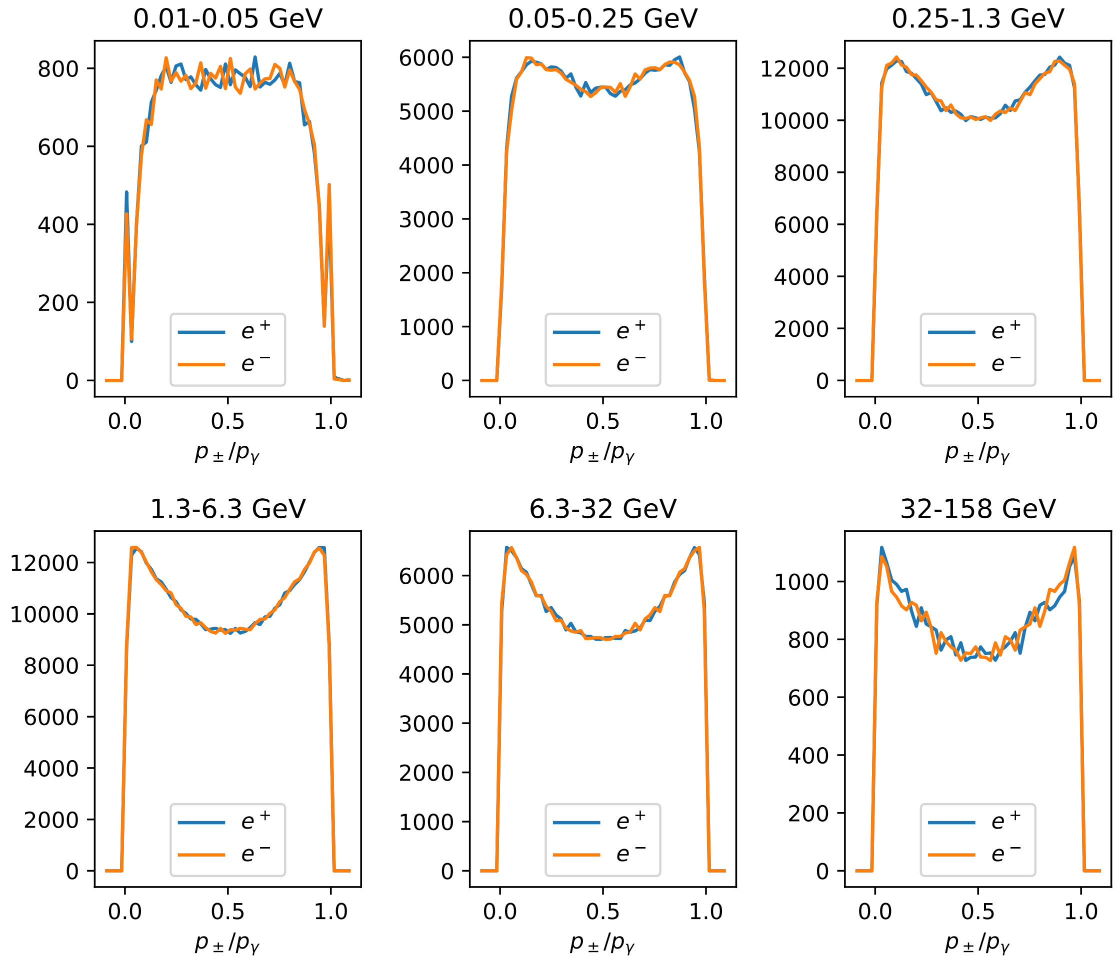

Figure 4.3: Histograms of the momentum fraction transferred to the electron and positron. The photon energies displayed above the plots are logarithmic intervals. From simulations with EPOS 1.99.

The energy distribution between the electron and positron significantly affects the analysis. NA61 can only detect particles with momenta above ~200 MeV/c. If the energy of one pair particle is less than 200 MeV, the pair will not be detected. For photons in the GeV range a significant fraction of the produced electrons and positrons is still below that threshold. Thus it is expected that the photon spectrum falls off for $E_\gamma \lesssim 10\,\text{GeV}$.

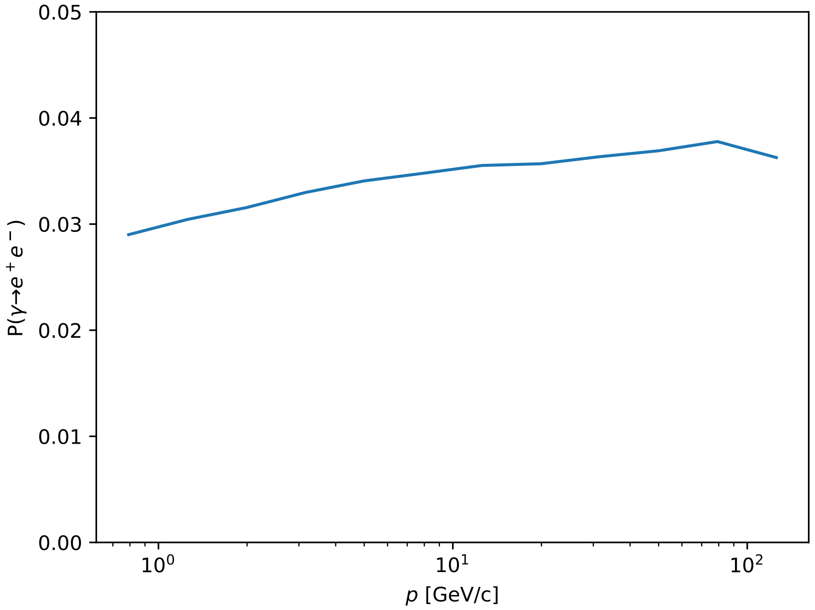

Figure 4.4: Energy dependence of the pair production probability in the detector simulation. From the full simulation with EPOS 1.99.

4.1.2 Pair Production Probability

Pair production happens when a photon interacts with a carbon nucleus in the target. The cross section can be obtained by integrating over Eq. (4.3) [25],

$$\sigma = \alpha Z^2 r_0^2 \left(\frac{28}{9} \ln\left(183 Z^{-\frac{1}{3}}\right) - \frac{2}{27}\right). \tag{4.4}$$

For carbon with $Z = 6$, the cross section is $\sigma = 298\,\text{mb}$. The target has a density of $\rho = 1.840\,\text{g/cm}^3$ and a length of $d = 2\,\text{cm}$. The interaction length is

$$\lambda_\gamma = \frac{M_\text{mol}}{N_A\,\rho\,\sigma} = 36.3\,\text{cm}. \tag{4.5}$$

With the molar mass $M_\text{mol} = 12\,\text{g/mol}$ of carbon and the Avogadro constant N_A. In a thin target, it can be assumed that the photons are produced at a random position in the target. After integrating over the target length, the pair production probability is

$$P_{\gamma\to e^+e^-} = \frac{1}{d}\int_0^d \left(1 - \exp\left(-\frac{x}{\lambda_\gamma}\right)\right) dx = 2.7\%. \tag{4.6}$$

In the simulation, the pair production probability is energy-dependent. This is likely due to additional material corrections applied to the cross section, see [26]. The average pair production probability for simulated photons above 1 GeV is $P_{\gamma\to e^+e^-} = 3.3\%$. The energy dependence is shown in Fig. 4.4.

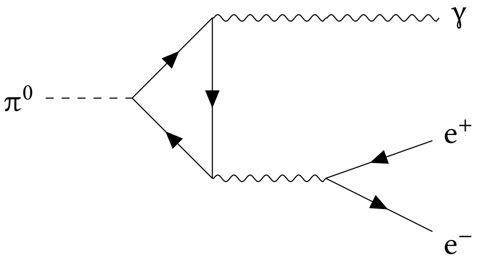

Figure 4.5: Diagram of a pion decaying into a photon and an electron-positron pair. In the two-photon process, the bottom right vertex is missing.

Table 4.1: Overview of the most important decay channels for photons and e^+e^- pairs. Branching ratios from [27].

source particle	channel	branching ratio
π^0	$\gamma\gamma$	98.8%
π^0	$e^+e^-\gamma$	1.2%
η	$\gamma\gamma$	39.4%
η	$\pi^+\pi^-\gamma$	4.3%
η	$e^+e^-\gamma$	0.7%

4.2 Source Particles

There are multiple sources of electron-positron pairs. The most important source is the pair production in the target. But the decays of neutral mesons produce e^+e^- pairs as well. Also, the photons themselves originate from meson decays. The relevant decay channels are listed in Table 4.1. The reconstruction of the simulated datasets suggests that most e^+e^- pairs from meson decays pass the invariant mass cut. This is reasonable since the processes in the $\gamma\gamma$ and $e^+e^-\gamma$ channels are almost the same. This is illustrated by the Feynman diagram in Fig. 4.5. This section discusses the production of photons and electron-positron pairs in the target.

4.2.1 Pion Decay

Neutral pions can decay into two photons or a photon and an electron-positron pair. The photon spectrum can be derived from the kinematics of the pion decay, see [1] for a full derivation. In the rest frame, the two photons are emitted in opposite directions with $E'_\gamma = \frac{1}{2} m_\pi c^2$. After a boost with $\beta = \frac{v}{c}$ into the lab system, the photon energy is

$$E_\gamma = \frac{E_\pi}{2} \left(1 - \beta \cos\theta\right) . \tag{4.7}$$

Here θ is the angle between the photon and pion directions. Since the decay is isotropic, the resulting spectrum is flat between the maximum and minimum energies,

$$\frac{dn_\gamma}{dE}(E) = \frac{2}{\beta E_\pi} \quad \text{for} \quad \frac{E_\pi}{2}(1-\beta) < E < \frac{E_\pi}{2}(1+\beta). \tag{4.8}$$

$\beta \approx 1$ for energies $E_\pi > 1\,\text{GeV}$ and the spectrum simplifies to

$$\frac{dn_\gamma}{dE}(E) = \frac{2}{E_\pi}\Theta\left(E_\pi - E\right). \tag{4.9}$$

This is the spectrum for a single pion with energy E_π. For N pions with energies $E_\pi^{(i)}$, the spectrum is

$$\frac{dn_\gamma}{dE} = \sum_{i=1}^{N} \frac{2}{E_\pi^{(i)}}\Theta\left(E_\pi^{(i)} - E\right) \overset{N\to\infty}{=} \int_E^\infty \frac{2}{E_\pi}\frac{dn_\pi}{dE}(E_\pi)dE_\pi. \tag{4.10}$$

Here $\frac{dn}{dE_\pi}$ is the pion spectrum. The equation can be solved for the pion spectrum,

$$\frac{dn}{dE_\pi}(E) = -\frac{E}{2}\frac{\partial}{\partial E}\frac{dn_\gamma}{dE}(E). \tag{4.11}$$

For a measured spectrum this is not practical. Nonetheless, Eq. (4.10) can be used to compare predicted pion spectra with measured photon spectra.

Simpler methods, like counting photons to calculate the pion number, are still challenging. Photons can only be detected down to a threshold energy E_0. Thus pions with energies below E_0 do not contribute to the spectrum. Additionally, pions with energies in the order of E_0 contribute only partly to the spectrum. For the threshold energy E_0, the average number of photons for a pion with energy E_π is

$$f(E_\pi) = \int_{E_0}^{E_\pi} \frac{2}{E_\pi}dE = 2\frac{E_\pi - E_0}{E_\pi}. \tag{4.12}$$

Without knowledge about the shape of the pion spectrum, it is not possible to compute this factor for all pions. For energies far above the threshold, the factor can be seen as constant $f = 2$. The threshold energy of NA61 for photons is about $E_0 = 2\,\text{GeV}$. This is too high for a reasonable analysis in the measured energy range.

4.2.2 Pair Spectrum Contribution

The measured electron-positron spectrum consists of pairs from meson decay and from pair production. Their ratio differs from the branching ratio since photons have to produce e^+e^- pairs before they can be detected. The number of pairs $N^\pi_{e^+e^-}$ produced from a pion is

$$N^\pi_{e^+e^-} = 2\Gamma_{\pi^0\to\gamma\gamma}P_{\gamma\to e^+e^-} + \Gamma_{\pi^0\to e^+e^-\gamma}P_{\gamma\to e^+e^-} + \Gamma_{\pi^0\to e^+e^-\gamma}. \tag{4.13}$$

Here $\Gamma_{a\to b}$ are the branching ratios for the respective decays from Table 4.1. The first term describes the decay into two photons. Both photons have to produce an e^+e^- pair in the target to be detected. The decay into a photon and an electron-positron pair requires the photon to produce a pair (second term), but the e^+e^- can be detected directly (third term). With $P_{\gamma\to e^+e^-} = 3.3\%$ and the values from Table 4.1 this results in

$$N^{\pi}_{e^+e^-} = 0.0776. \tag{4.14}$$

About 16% of the pairs come from the $\pi^0 \to e^+e^-\gamma$ channel even though its branching ratio is only 1.2%. For etas, the number is

$$N^{\eta}_{e^+e^-} = 2\Gamma_{\eta^0\to\gamma\gamma}\, P_{\gamma\to e^+e^-} + \Gamma_{\eta\to e^+e^-\gamma}\, P_{\gamma\to e^+e^-} + \Gamma_{\eta\to e^+e^-\gamma} + \Gamma_{\eta\to\pi^+\pi^-\gamma}\, P_{\gamma\to e^+e^-}. \tag{4.15}$$

Here an additional term for the $\eta \to \pi^+\pi^-\gamma$ channel is required. The numerical value is $N^{\eta}_{e^+e^-} = 0.0347$. In the simulation, the η to π^0 ratio is 13% resulting in about 6% of the pairs coming from etas. The ratio cannot be measured, thus proving another difficulty in the pion spectrum reconstruction.

4.2.3 Direct Pion Measurement

It was proposed in [28] to measure pions based on the invariant mass of an electron quadruplet. Since the $\pi \to e^+e^-e^+e^-$ channel is negligible, only the channels discussed before contribute to the quadruplet number,

$$N^{\pi}_{e^+e^-e^+e^-} = \Gamma_{\pi^0\to\gamma\gamma}\, P^2_{\gamma\to e^+e^-} + \Gamma_{\pi^0\to e^+e^-\gamma}\, P_{\gamma\to e^+e^-} = 0.00147. \tag{4.16}$$

Since the two-photon channel is even more suppressed, 27% of the quadruplets come from the $\pi^0 \to e^+e^-\gamma$ channel. As expected the quadruplet number is significantly less than the pair number. Additionally, detection thresholds now apply to all four particles. Pions decaying into a low and a high energy photon cannot be detected by this method. Similar to Eq. (4.12) the fraction of detectable pions depends on the shape of the spectrum. If the spectrum of the detected pions could be reconstructed with this method, the detection probability can be calculated. This would allow us to acquire the actual pion spectrum.

Figure 4.6 shows the invariant mass distribution of electron quadruplets. All combinations of two positive and two negative particles in an event are formed. The invariant mass histogram is fitted with two fit functions [28]:

$$a(m) = \frac{\kappa}{\sqrt{2\pi\sigma^2}} \exp\left(-\frac{(m-\mu)^2}{2\sigma^2}\right) \tag{4.17}$$

$$b(m) = A + Bm + Cm^2 + Dm^3 \tag{4.18}$$

A signal area $S = [0.06, 0.2]$ GeV is defined. The background function $b(m)$ is fitted outside of S. $b(m)$ is then extrapolated into S and subtracted from the histogram. The signal function $a(m)$ is then fitted to the remainder in S. $a(m)$ is a normal distribution around μ

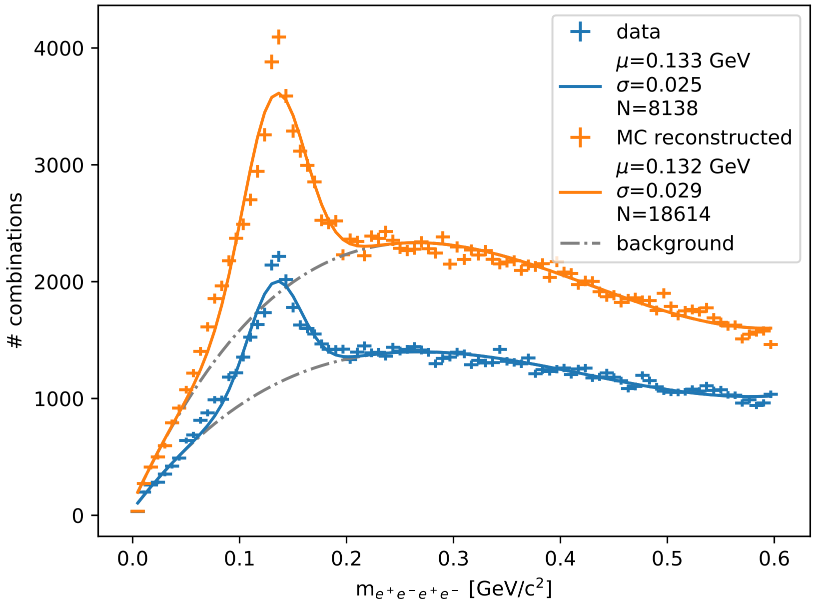

Figure 4.6: Histogram of the invariant mass of electron quadruplets. A two-component fit consisting of signal and background is shown as a solid line. The fit parameters are in the legend, for the fit functions see Eq. (4.17) and Eq. (4.18).

Table 4.2: The number of pions obtained from electron quadruplets.

dataset	N_π
reconstructed data	8 138
reconstructed simulation (EPOS 1.99)	18 614
reconstructed simulation (QGSJet II-04)	17 326

with variance σ^2. If the signal is from pion decay, μ will be the pion mass (135 MeV). The number of pions N_π can be calculated from the normalization constant κ as

$$N_\pi = \frac{\kappa}{\Delta m}. \tag{4.19}$$

Simply counting the signal events yields a similar value by 1%. The resulting pion numbers can be found in Table 4.2.

The results reveal two interesting aspects. First, there are less pions in the data than in the simulation. Even after normalization, the data contains 52% less pions. Second, since background and signal events cannot be individually separated, no spectrum can be obtained. Splitting the analysis into multiple momentum bins is possible, but difficult due to the low statistics.

The quadruplet analysis can be applied to etas as well. The quadruplet number for etas is

$$N^{\eta}_{e^+e^-e^+e^-} = \Gamma_{\eta\to\gamma\gamma}\, P^2_{\gamma\to e^+e^-} + \Gamma_{\eta\to e^+e^-\gamma}\, P_{\gamma\to e^+e^-} = 0.00066. \tag{4.20}$$

With the numbers from the simulation, this should result in an eta peak 5.8% the size of the pion peak. This corresponds to 1 355 etas in comparison to about 25 000 events in the 100 MeV/c^2 region around the eta mass. No eta peak can be seen in Fig. 4.6. A fit attempt was not performed.

4.2.4 Feasibility Considerations

The discussed aspects indicate that further analysis is quite challenging. A reconstruction of the photon and pion spectra requires overcoming the following obstacles:

1. Distinguishing between electron-positron pairs from different source particles.
2. Resolving the relationship between the photon and pion spectra.
3. Measuring the pion to eta ratio.
4. Removing the background from the quadruplet analysis.

Nonetheless, measuring the electron-positron spectrum is quite fruitful. Since the photon spectrum can be obtained from the pion spectrum, it can be easily produced from the pion predictions of hadronic interaction models. The e^+e^- pair spectrum can be calculated with the production probability and the known branching ratios. This allows a comparison between hadronic interaction models and the measured spectrum.

4.3 Data and Reconstruction

The data used in this analysis is the same as the one used in [11]. A beam consisting of negatively charged pions with a momentum of 158 GeV/c hits a 2 cm graphite target. It is delivered by the SPS in the H2 beamline. As described in Section 2.1, the π^- originate from the T2 target. The T2 target is a 10 cm beryllium plate and the primary particles are 400 GeV protons. The CEDAR selects the negative pions, the beam trigger and the interaction trigger are used, see Section 2.2. The target density is $\rho = 1.840\,\mathrm{g/cm^3}$. 5.5 million events were recorded.

The data is available as SHINE offline event (SHOE) files, the internal data format of the SHINE offline framework [23]. These files contain lists of events. For each event, the quality is checked the same way as in [11]. Bad events are excluded from the reconstruction. Examples of bad events are events with multiple or noncentral beam particles. Each event contains a list of tracks. Tracks are the trajectories of particles through the TPCs. They consist of clusters, the three-dimensional charge deposits measured by the TPCs. Each track has a momentum, a charge and an energy deposit. The tracks were reconstructed by the SHINE offline framework by fitting for the track momentum that best describes the trajectory of the particle. The tracks were then fitted to a common point of origin, the main vertex. Based on the track topology, the number of clusters and the fit quality, cuts are applied. For example, tracks at the edges of the TPCs and tracks with too few clusters are removed. The cuts ensure that only well-reconstructed tracks are analyzed. Possible errors and uncertainties introduced by these cuts are discussed in Section 4.6.

4.3.1 Simulation

Not only measured data but also simulated data is available for π^--C interactions. The simulations are available as SHOE files as well. They were generated by the detector simulation with GEANT 3.21 [29]. The π^--C interactions originate from CRMC simulations [30] using the models EPOS 1.99 [31] and QGSJet II-04 [32]. EPOS and QGSJet are hadronic interaction models. They predict what will be measured in the experiment. A major goal of the measurement is to improve the models by adjusting them to the measured data. How using those models for simulations affects the results is discussed in Section 4.6. The same models are used in extensive air shower simulations.

The SHOE files from simulations contain additional information. They especially contain simulated tracks that can be matched to the reconstructed tracks. Simulated tracks contain information about the true momenta and the particle species. This is the basis for the particle identification in Section 4.4. Additionally, simulated tracks start in the target. This allows us to figure out their origin and parent particle.

The simulation files are treated the same way as the data files. In addition to the charge, momentum and energy deposit, the particle species, parent particle and origin z-position are extracted from the SHOE files. This is used later to find reasonable cuts for particle and pair identification. To allow an extensive study of pair production and reconstruction efficiency, all electron-positron pairs are extracted from the simulation. They are stored as an independent dataset.

4.3.2 Datasets

In the following sections, three datasets are used. They differ in how pairs are reconstructed. The first dataset contains pairs from the reconstructed data. For each event, every positive particle identified as a positron is matched with every negative particle identified as an electron. So every possible combination of electrons and positrons is generated. This guarantees that all actual pairs are reconstructed, but it can produce additional unwanted pairs. Each pair consists of the momenta of the two particles. The second dataset contains pairs from the reconstructed simulation with EPOS 1.99. The pairs are generated the same way, but they are split into a *pair* and *nopair* subset for actual and wrong pairs respectively. The *nopair* subset includes pairs produced outside of the target. The third dataset consists of all simulated pairs produced in the target. Each pair is traced back to the particle it originated from, creating a tree-like data structure. This dataset contains the simulated

Table 4.3: List of datasets. The reconstructed data has no distinction between actual and wrong pairs. The reconstructed simulation is from simulations with EPOS 1.99.

dataset	*pair*	*nopair*
reconstructed data	425 037	
reconstructed simulation	246 970	336 877
full simulation	1 646 981	0

Table 4.4: Scale factor, efficiency and purity for positrons and electrons. The efficiency is the number of electrons inside the partition divided by all electrons. The purity is the electron number divided by all particles in the partition.

particle	f	efficiency	purity
positron	30	98%	54%
electron	40	97%	56%

momenta of the particles and is used as Monte Carlo truth. Table 4.3 lists the properties of the three datasets.

4.4 Particle Identification

Charged particles traveling through matter lose energy by ionization. Figure 4.7 shows the energy loss of particles in the TPCs and their momenta. The solid lines follow a parameterized version of the Bethe formula [11, 33]. It is possible to identify different particles by their energy loss. For this the $\frac{dE}{dx}$-p space is partitioned into areas, based on how likely a particle in this area belongs to a specific species. The partitioning is based on the simulation with EPOS. There it is possible to count the number of each particle species per $\frac{dE}{dx}$-p bin.

The most common particle in each bin can be chosen as bin species. This would yield a high purity for electrons and positrons. Unfortunately, this removes many positrons in the proton and pion crossing regions. For the following analysis, a high positron efficiency is needed. This requires including bins, in which positrons are not the most common particles. The partitioning used hereafter is shown in Fig. 4.8. Here a bin is counted as a positron bin if the number of positrons times a factor f is larger than all other particle numbers. For electrons, there is no proton crossing, but the pion crossing happens as well. Thus for electrons, the same method is applied. The factors are chosen to yield a high efficiency while still keeping the majority of particles to be electrons and positrons. Table 4.4 summarizes the scale factors, efficiencies and purities. These values are calculated based on the simulation with EPOS. The simulation with QGSJet results in comparable efficiencies. For the data these values are unknown.

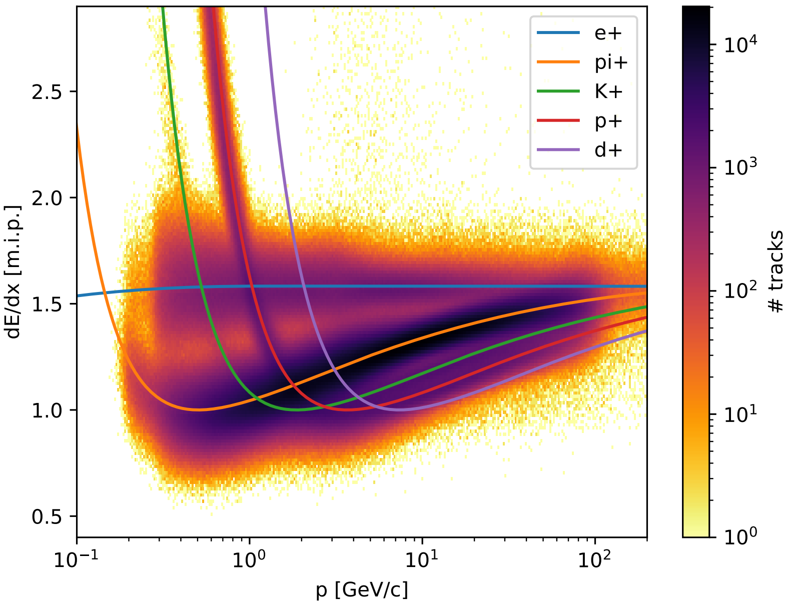

Figure 4.7: Two-dimensional histogram of reconstructed momentum and energy loss in the TPCs. The solid lines are a parametrization of the energy loss based on the Bethe formula.

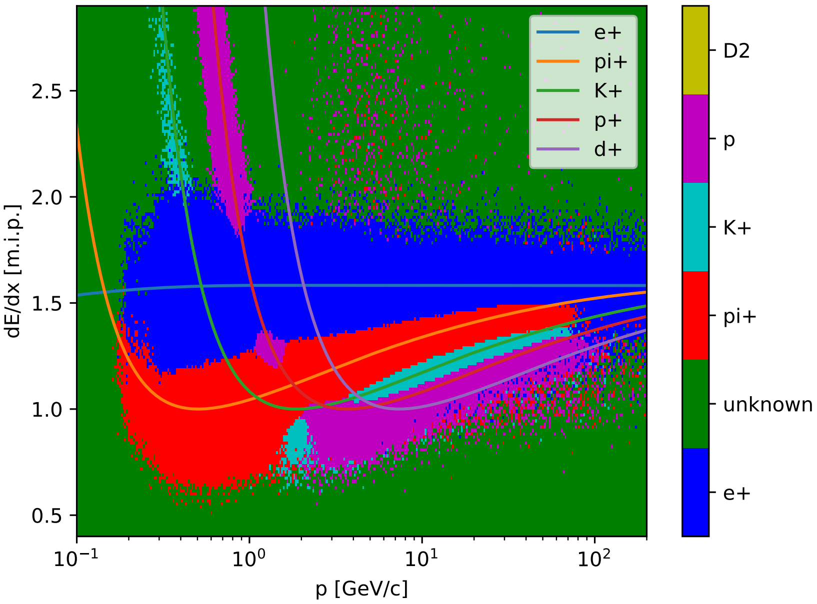

Figure 4.8: Partitioning of the $\frac{dE}{dx}$-p space into different particle species for positive charge.

4.5 Invariant Mass Cut

To reconstruct photons, it is necessary to find pairs of electrons and positrons and to check if they are from a photon. Additionally, it is necessary to ensure the pair originates from the target. The pair production probability inside the target is about 3.3% for photons above 1 GeV. This was derived from simulations by counting the number of pairs and photons in the target. See Section 4.1.2 for an analytical derivation. Aside from the target, pair production can happen everywhere in the detector. Excluding pairs produced in the detector is necessary since their production probabilities are unknown. Both criteria can be fulfilled by an invariant mass cut. The invariant mass m of a particle is defined as

$$m^2 = E^2 - \vec{p}^2. \tag{4.21}$$

The invariant mass of a photon is zero. If only a small amount of energy is transferred to a nucleus in pair production, the e^+e^- pair will carry approximately the photon energy and momentum. Thus the invariant mass of the electron-positron pair is close to zero as well.

Electron-positron pairs can be produced outside of the target. The track reconstruction algorithm fits all particle tracks to the main vertex, which is inside the target. If a particle originates from outside the target, its momentum will be reconstructed wrong. Thus the invariant mass of a pair produced outside the target deviates from zero. Therefore, out-of-target pairs are suppressed by the cut as well.

In the analysis, all positive particles are matched with all negative particles in an event. The resulting pairs can be electron-positron pairs from pair production. If they are, they are expected to have an invariant mass close to zero. Pairs without a common origin have a random invariant mass. Pion pairs that are accidentally identified as e^+e^- pairs have much higher masses. Figure 4.9 shows the distribution of the reconstructed invariant mass from simulations. It is evident, that the invariant mass can be used to differentiate between actual e^+e^- pairs and other combinations.

Figure 4.10 shows the distribution of the reconstructed invariant mass in dependence on the pair momentum. It can be seen that it spreads out for higher momenta. The algorithm that reconstructs the momenta of the particles uses the bending of the tracks in the magnetic field. Thus the reconstructed quantity is $\frac{1}{p}$. This results in a reduced momentum resolution for higher momenta. Since the invariant mass calculation relies on a good momentum reconstruction, it gets less precise for high momenta. To achieve comparably high efficiency over the entire momentum range, a momentum-dependent invariant mass cut is chosen. The cut – indicated by a solid line in Fig. 4.10 – is defined as

$$m^2 < m_0^2 p^\alpha. \tag{4.22}$$

m is the invariant mass of the pair in GeV/c^2 and p is the pair momentum in GeV/c. The constants are $m_0^2 = 4.851 \cdot 10^{-4}$ and $\alpha = 0.7$. α was chosen to yield the best actual to wrong pair ratio. This was done by selecting different values for α and calculating m_0^2 so that 5%

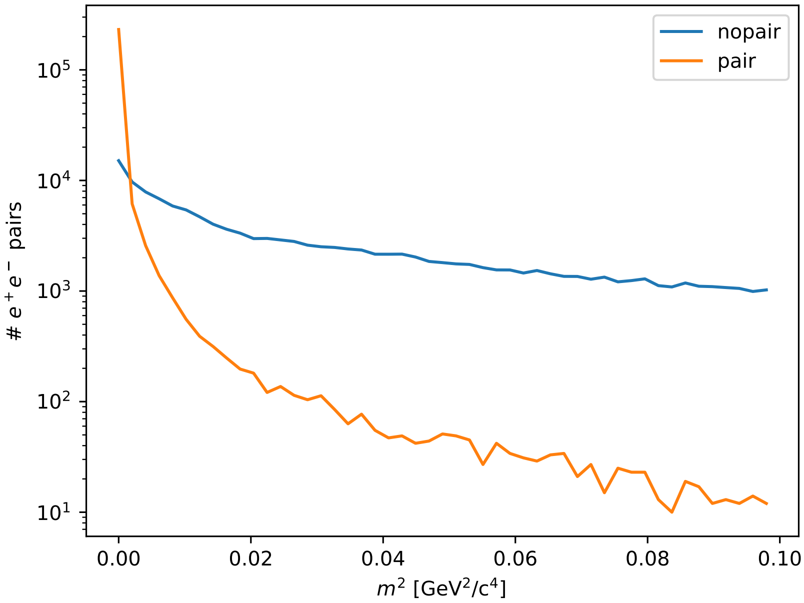

Figure 4.9: Histogram of the invariant mass from actual e^+e^- pairs compared to other combinations. The histogram contains 99.7% of the actual pairs, but only 40% of the wrong pairs. From the reconstructed simulation with EPOS 1.99.

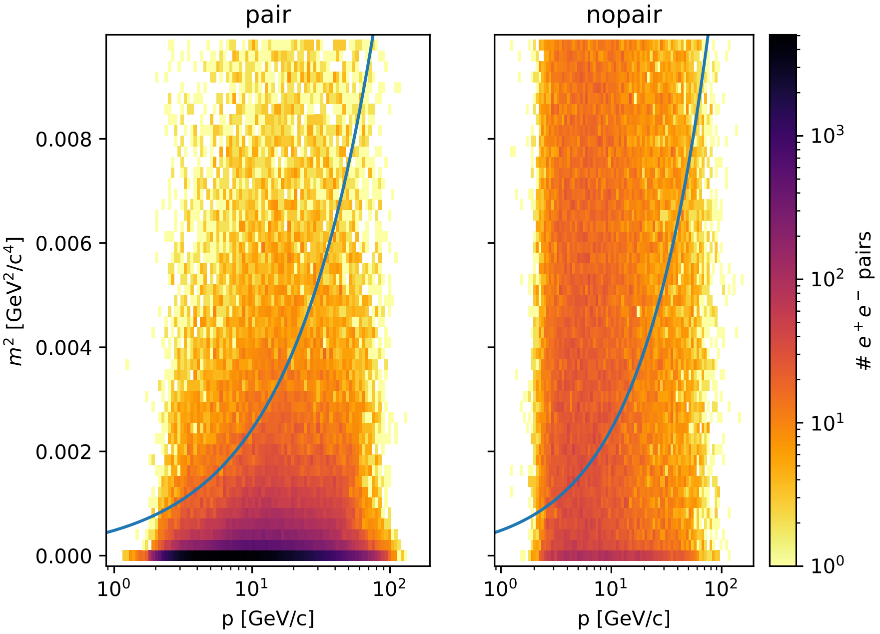

Figure 4.10: 2D-histogram of the invariant mass by momentum. The left histogram shows actual pairs, the right shows wrong pairs. The solid line is the invariant mass cut. From the reconstructed simulation with EPOS 1.99.

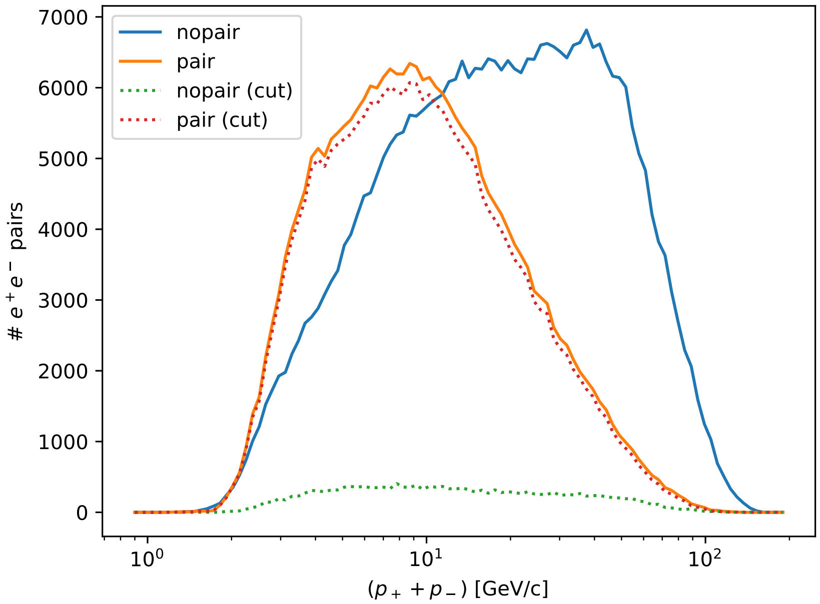

Figure 4.11: Spectra of actual and wrong pairs before and after the invariant mass cut. From the reconstructed simulation with EPOS 1.99.

of the wrong pairs pass the cut. The value for α that yielded the highest efficiency was chosen. The resulting efficiency is 95% for the simulation with EPOS 1.99.

With the invariant mass cut, a first e^+e^- pair spectrum can be obtained. The spectrum is shown in Fig. 4.11 for the simulation. While the wrong pairs dominate the higher momenta, they are efficiently suppressed by the cut. Most actual pairs pass the cut for low momenta, while there are inefficiencies at higher momenta, see Fig. 4.12. In general, the shape is mildly distorted, but the background suppression is strong over the entire momentum range.

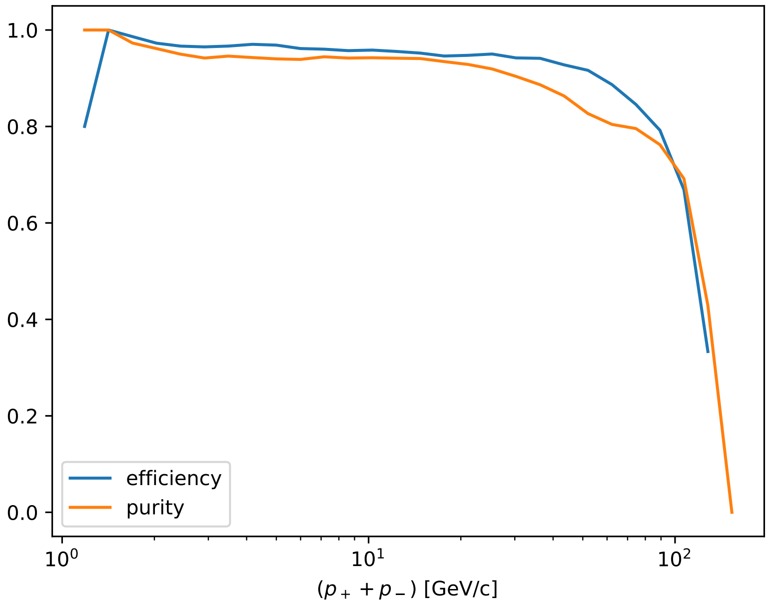

Figure 4.12: Efficiency and purity of the invariant mass cut in dependence of the pair momentum. From the reconstructed simulation with EPOS 1.99.

4.6 Corrections

In the previous section, a method to reconstruct electron-positron pairs was discussed. The resulting spectra show absolute numbers with no physical importance. To allow further discussion of the results, a normalized, comparable quantity is needed. This quantity is the average multiplicity,

$$\frac{dn}{dp} = \frac{N(p)}{\Delta p \, N_{\text{events}}}. \tag{4.23}$$

Here $N(p)$ is the number of particles in a bin of size Δp and N_{events} the number of events. This section describes how to calculate the average multiplicity of e^+e^- pairs leaving the target, Section 4.2 discusses how to obtain the photon spectrum. To improve the readability of the plots at large momenta, the quantity $p\frac{dn}{dp}$ is shown in the figures.

The pair spectrum $N(p)$ is the true number of pairs in an interval of size Δp around the true momentum p. The reconstructed spectrum $N_r(p_r)$ is the number of reconstructed pairs in an interval around the reconstructed momentum p_r. Four corrections are needed to get from $N_r(p_r)$ to $N(p)$:

1. The trigger bias correction yields a trigger-independent spectrum per event. (see Section 4.6.1)
2. The pair correction corrects for misidentified pairs. (see Section 4.6.2)

3. The bin migration correction turns the reconstructed momentum into the true momentum. (see Section 4.6.3)
4. The efficiency correction corrects for the detector sensitivity and the quality and acceptance cuts. (see Section 4.6.4)

Each step yields a correction factor and an uncertainty. All factors are multiplied with $N_r(p_r)$ to get the final result. For comparability a normalization factor

$$S = \frac{p}{\Delta p \, N_{\text{events}}} \tag{4.24}$$

is applied to $N_r(p_r)$ at the beginning. This factor converts all numbers to multiplicities. Due to the logarithmic binning ($\Delta \propto p$), it is a constant. The total correction is

$$p\frac{dn}{dp}(p) = S\,E(p)\,P(p_r)\,T(p_r)\,N_r(p_r). \tag{4.25}$$

The correction factors are shown in Fig. 4.13 and discussed in the following sections. Note that the product of E, P and T yields a combined correction factor,

$$C = \left(\frac{N^s(p)}{N^s_{\text{events}}} \middle/ \frac{N^t_r(p_r)}{N^t_{\text{events}}} \right). \tag{4.26}$$

Here $N^s(p)$ is the simulated spectrum and $N^t_r(p_r)$ is the reconstruction of the simulated spectrum. The factor is split into different contributions to make the evaluation of uncertainties easier.

4.6.1 Trigger Bias

The data was taken with the interaction trigger, see Section 2.2. This trigger ensures that only events in which an interaction happens are recorded. It uses the scintillator S4 which is placed in the beamline between the TPCs. Not only the beam particle, but all particles with high momenta can hit S4. Additionally, low-momentum particles with high transverse momentum can be bent by the magnetic field to hit S4 as well. Events containing such particles are removed by the interaction trigger. To correct this effect, called trigger bias, a correction is needed.

In the simulations, N^s_{events} events are simulated, but only N^t_{events} are triggered. The triggered spectrum $N^t_r(p_r)$ is related to the simulated spectrum $N^s_r(p_r)$ by a factor $T(p_r)$, which is defined by

$$\frac{N^s_r(p_r)}{N^s_{\text{events}}} = T(p_r)\frac{N^t_r(p_r)}{N^t_{\text{events}}}. \tag{4.27}$$

The trigger bias factor $T(p_r)$ is momentum-dependent since events with high momentum particles are removed by the interaction trigger. These events are added back by the trigger bias correction. For most other events, it is only a change in the normalization. Figure 4.13

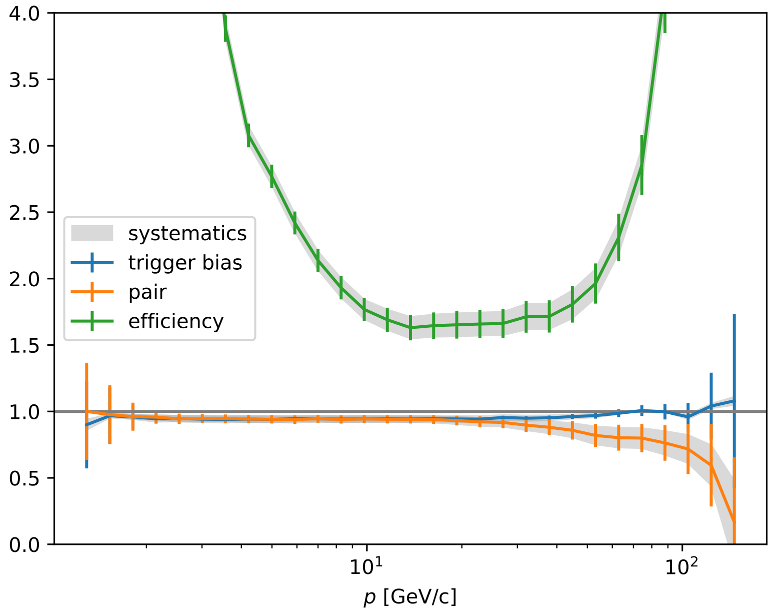

Figure 4.13: The different correction factors as a function of the momentum. Statistical uncertainties are shown as error bars and systematic uncertainties as a grey band.

shows the trigger bias factor as a blue line. It is mostly constant and smaller than one except for high momenta.

The statistical uncertainty arises from the finite number of simulations. With Poissonian statistics and standard propagation of uncertainties, the statistical uncertainty is

$$\sigma_T(p_r) = T(p_r)\sqrt{\frac{1}{N_r^s(p_r)} + \frac{1}{N_r^t(p_r)}}. \tag{4.28}$$

The trigger bias factor is model-dependent. The model uncertainty is estimated as the difference between the model and the data. It is set to the average relative difference $f_m = 37\%$. The systematic uncertainty of $T(p_r)$ is

$$f_T(p_r) = f_m|1 - T(p_r)|. \tag{4.29}$$

Both uncertainties are small for most momenta. For high and low momenta, where statistics are low, the statistical uncertainty increases.

4.6.2 Pair Correction

Not all electron-positron pairs pass the invariant mass cut. But a small number of wrong pairs pass the cut, see Fig. 4.11. The number of actual and wrong pairs is not independent of each other. Thus a common correction is used to correct for both effects. The pair correction factor $P(p_r)$ is defined as

$$N_p^s(p_r) = P(p_r)N_r^s(p_r). \tag{4.30}$$

$N_p^s(p_r)$ is the spectrum of the reconstructed actual pairs in the simulation. $P(p_r)$ is shown in orange in Fig. 4.13. It is smaller than one since the efficiency of the invariant mass cut is better than its purity. Up to about 20 GeV/c it remains almost constant For higher momenta, it decreases since the purity gets worse.

The statistical uncertainty is calculated equivalent to Eq. (4.28). It increases for low and high momenta where statistics are low. The systematic uncertainty is model-dependent and calculated the same as Eq. (4.29). Since the pair correction gets stronger for higher momenta, the uncertainty increases as well. For lower momenta the systematic uncertainty is small.

4.6.3 Bin Migration

The reconstructed momentum of a pair differs from its true momentum due to the momentum resolution of NA61. The uncertainty of the reconstructed momentum depends on the momenta of the electron and positron. All information about them is lost when the pairs are binned. For binned data, an effect called bin migration is considered instead. A pair can be within a bin that contains its true momentum. But it can also be in a neighboring bin. If it is, the number of pairs in the true bin is reduced while the number in the neighboring bin is increased. The number of pairs leaving a bin only depends on the bin itself. However, the number of pairs entering a bin depends on the neighboring bins as well. Thus the bin migration is a model-dependent effect. For a reasonable bin size – one that is larger than the momentum resolution – bin migration is small. Therefore the bin migration is not explicitly corrected but added as a systematic uncertainty instead,

$$f_M(p) = f_m|N_p^s(p) - N_p^s(p_r)|. \tag{4.31}$$

For the following corrections the pair spectrum is considered to be a function of the true momentum,

$$N_p^s(p) = N_p^s(p_r) \qquad p = p_r. \tag{4.32}$$

Reconstructed and true momentum are no longer distinguished.

4.6.4 Efficiency

NA61 has a larger width than height. Thus particles are more likely reconstructed when they are in the magnetic bending plane. Additionally, the sensitivity of NA61 rapidly drops off at the edges of the TPCs. To only analyze regions of the detector in which almost all particles are reconstructed, an acceptance cut is defined. Based on their momentum and track topology particles are either accepted or rejected. The acceptance cut is from

[11]. It can be corrected by using the full simulated spectrum $N^s(p)$ and relating it to the reconstructed spectrum like

$$N^s(p) = E(p)N^s_p(p). \tag{4.33}$$

All physical processes considered in this analysis possess rotational symmetry. Thus the spectrum does not depend on the angle perpendicular to the beam axis. This results in the correction being purely geometrical. But both the correction and the acceptance are momentum-dependent. This accounts for the sensitivity limits of NA61. In contrast to the sharp limits on individual particles, the sensitivity for pair reconstruction continually falls off. This is the case for high and low momenta. Here electrons and positrons gradually leave the acceptance. The correction is shown in green in Fig. 4.13. It is called the efficiency correction factor.

The statistical uncertainty is calculated similarly to Eq. (4.28). The systematic uncertainty is model-independent. In the case of a purely geometrical correction, it can be considered to be zero. If tracks are lost within the acceptance, they will be corrected with the simulated tracking efficiency. In [11] the loss of tracks inside the acceptance is considered to be negligible. Therefore the systematic uncertainty threaded as purely geometrical. The systematic uncertainty shown in Fig. 4.13 is the bin migration uncertainty. The bin migration is implicitly corrected since the simulated spectrum uses true momenta.

4.7 Results

Figure 4.14 shows the measurement of the e^+e^- pair spectrum after the target. The discussed correction factors were applied. It can be compared with the spectra from models. The models shown are EPOS 1.99 [31] and QGSJet II-04 [32]. As it can be seen in Fig. 4.14, the model and the data do not agree with each other.

Both models predict about 30% more electron-positron pairs than measured. Possible systematic uncertainties that were not considered, like the feed-down from secondary interactions, are considered to be too small to explain the differences. While the comparison at this stage does not reveal why there are differences, it makes clear they are significant. A comparison with other hadronic interaction models is possible by extracting their electron and photon spectra. The photon spectrum has to be multiplied by the pair production probability. This makes this result usable for model tuning.

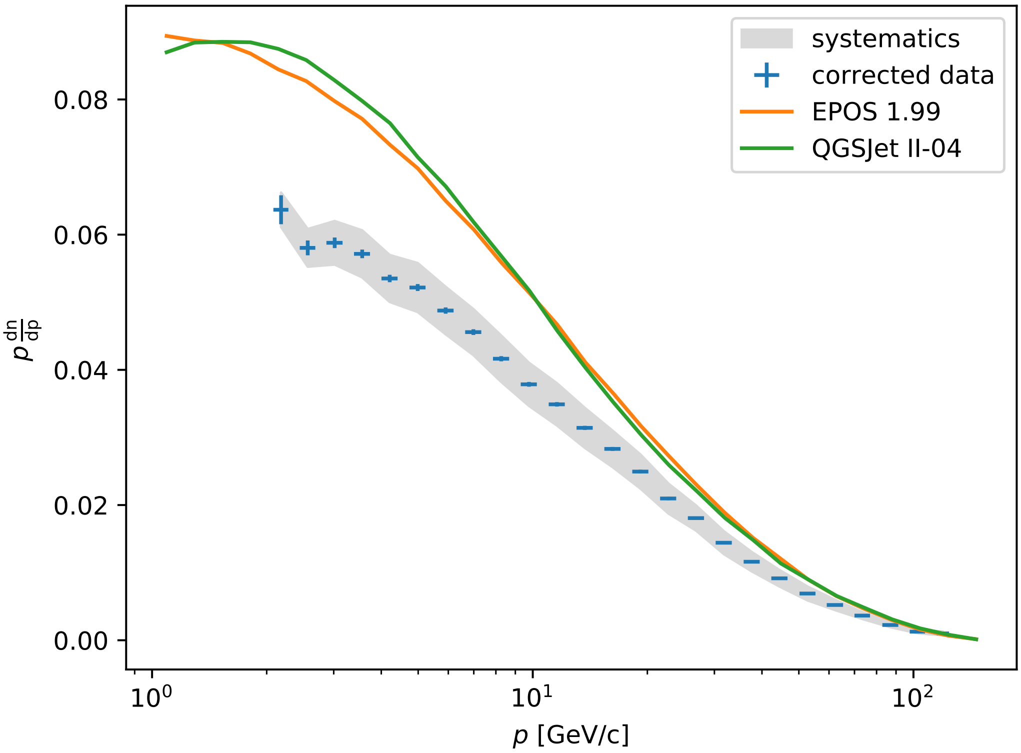

Figure 4.14: The e^+e^- pair spectrum obtained from the measurement with all corrections applied. Statistical uncertainties are shown as error bars and systematic uncertainties as a grey band. The resulting spectrum is compared with the hadronic interaction models EPOS 1.99 and QGSJet II-04.

5 Summary

In this thesis, two studies related to the understanding of cosmic ray propagation in the Galaxy and cosmic ray–induced air showers were presented. Concerning the first topic, theoretical studies were performed in preparation for a future fragmentation measurement. One of them separated the interaction probabilities upstream, downstream and in the target. An extensible method to construct analytical expressions for these probabilities was presented. This will be important for future data taking to analyze the production of light isotopes like beryllium and lithium. To extract the interaction probability in the target, an estimation of the upstream probabilities is needed. This thesis proposes to calculate them based on the simultaneously measured survival probabilities of the particles. With this method, the largest systematic uncertainty in the analysis of the pilot run data from 2018 can be reduced significantly. The new method was already applied to the latest release of the pilot run data, removing a relative systematic uncertainty of 3% [14]. Furthermore, an analytical description of processes inside the target was developed. Instead of the simple linear approximation used in the previous analysis, the full solution of the differential equation was derived. For this, a matrix containing the interaction lengths was introduced. The solution can be evaluated with the help of a computer algebra system. This allows us to quantify the effects of feed-down and destruction caused by secondary interactions. Not only does this reduce the systematic uncertainty of the measurement, but it enables us to use a target with optimal thickness as well. This thesis proposes that the gain in interactions from a relatively thick target outweighs the complications arising from secondary interactions. In particular, the relevant secondary interactions can be calculated from auxiliary measurements to eliminate systematic uncertainties. A method to optimize the target thickness using the full analytical description of the target was developed. This method shows that the uncertainties of the desired cross sections can be reduced by using a thicker target.

Since the data taking with a fragmented beam expected for late 2022 was delayed to 2024 the second part of the thesis was devoted to a different topic. In this part, the electromagnetic component in extensive air showers was studied. For that purpose, the measurement of neutral pion production in π^-+C interactions at 158 GeV recorded in 2009 was investigated. Electrons and positrons were identified by their energy loss in the TPCs. To achieve a high electron efficiency, an energy loss–momentum histogram was partitioned into different areas for different particles. Pairs of electrons and positrons were identified by a momentum-dependent invariant mass cut. An extensive study of their sources – the pair production from photons and neutral meson decays – was conducted to ensure the comparability with hadronic interaction models at the generator level. Inefficiencies of the detector and trigger setup were corrected with correction factors derived from simulations. The final result was compared with model predictions. It revealed that the hadronic interaction models EPOS 1.99 and QGSJet II-04 overestimate the electromagnetic component by up to 30%. This result provides direct evidence that the muon deficit might be caused by an overprediction of the electromagnetic component in hadronic interaction models.

Bibliography

[1] T. K. Gaisser, R. Engel, and E. Resconi. *Cosmic Rays and Particle Physics.* 2nd ed. Cambridge University Press, 2016. DOI: `10.1017/CBO9781139192194`.

[2] Carmelo Evoli. *The Cosmic-Ray Energy Spectrum.* Dec. 2020. DOI: `10.5281/zenodo.4396125`.

[3] S. G. Mashnik. “On solar system and cosmic rays nucleosynthesis and spallation processes” (). arXiv: `astro-ph/0008382`.

[4] M. S. Longair. *High Energy Astrophysics.* 3rd ed. Cambridge University Press, 2011. DOI: `10.1017/CBO9780511778346`.

[5] A. Reinert and M. W. Winkler. “A Precision Search for WIMPs with Charged Cosmic Rays”. *JCAP* 01 (2018), p. 055. DOI: `10.1088/1475-7516/2018/01/055`. arXiv: `1712.00002 [astro-ph.HE]`.

[6] D. Heck et al. “CORSIKA: A Monte Carlo code to simulate extensive air showers”. *Report FZKA* 6019.11 (1998).

[7] J. Matthews. “A Heitler model of extensive air showers”. *Astropart. Phys.* 22.5-6 (2005). DOI: `10.1016/j.astropartphys.2004.09.003`.

[8] W. Heitler. *The quantum theory of radiation.* Vol. 5. International Series of Monographs on Physics. Oxford: Oxford University Press, 1936.

[9] H. P. Dembinski et al. “Report on Tests and Measurements of Hadronic Interaction Properties with Air Showers”. *EPJ Web Conf.* 210 (2019). Ed. by I. Lhenry-Yvon et al., p. 02004. DOI: `10.1051/epjconf/201921002004`. arXiv: `1902.08124 [astro-ph.HE]`.

[10] N. Abgrall et al. “NA61/SHINE facility at the CERN SPS: beams and detector system”. *JINST* 9.06 (), P06005–P06005. DOI: `10.1088/1748-0221/9/06/p06005`.

[11] H. Adhikary et al. “Measurement of hadron production in π–C interactions at 158 and 350 GeV/c with NA61/SHINE at the CERN SPS”. *Phys. Rev. D* 107.6 (2023), p. 062004. DOI: `10.1103/PhysRevD.107.062004`. arXiv: `2209.10561 [nucl-ex]`.

[12] F. Sutter. “Messung der Fragmentation von Kohlenstoff zu Bor bei einer Energie von 13.5 A GeV”. Masterarbeit. Karlsruher Institute für Technologie, 2019.

[13] M. Unger. “New Results from the Cosmic-Ray Program of the NA61/SHINE facility at the CERN SPS”. *PoS* ICRC2019 (2020), p. 446. DOI: `10.22323/1.358.0446`. arXiv: `1909.07136 [astro-ph.HE]`.

[14] N. Amin. “Pilot Study on the Measurement of the Production of Boron Isotopes in C+p Reactions at 13.5A GeV/c with NA61/SHINE”. *PoS* ICRC2023 (2023), p. 075. DOI: `10.22323/1.444.0075`.

[15] N. Amin. “Results from a Pilot Study on the Measurement of Nuclear Fragmentation with NA61/SHINE at the CERN SPS: ^{11}C Production in C+p Interactions at 13.5 A GeV/c”. *PoS* ICRC2021 (2021), p. 102. DOI: `10.22323/1.395.0102`. arXiv: `2107.12275 [nucl-ex]`.

[16] Y. Genolini et al. “Current status and desired precision of the isotopic production cross sections relevant to astrophysics of cosmic rays: Li, Be, B, C, and N”. *Phys. Rev. C* 98.3 (2018), p. 034611. DOI: `10.1103/PhysRevC.98.034611`. arXiv: `1803.04686 [astro-ph.HE]`.

[17] Y. Génolini et al. “Current status and desired accuracy of the isotopic production cross-sections relevant to astrophysics of cosmic rays II. Fluorine to Silicon (and updated LiBeB)” (). arXiv: `2307.06798 [astro-ph.HE]`.

[18] *BC-400/BC-404/BC-408/BC-412/BC-416 Premium Plastic Scintillators.* URL: `https://www.phys.ufl.edu/courses/phy4803L/group_I/muon/bicron_bc400-416.pdf`.

[19] G. D. Westfall et al. “Fragmentation of relativistic Fe-56”. *Phys. Rev. C* 19 (1979), pp. 1309–1323. DOI: `10.1103/PhysRevC.19.1309`.

[20] Wolfram Research, Inc. *Mathematica, Version 13.3.* 2023. URL: `https://www.wolfram.com/mathematica`.

[21] A. Ferrari et al. “FLUKA: A multi-particle transport code (Program version 2005)” (). DOI: `10.2172/877507`.

[22] N. Charitonidis. private communication. 2022.

[23] R. Sipos et al. “The offline software framework of the NA61/SHINE experiment”. *J. Phys. Conf. Ser.* 396 (2012). Ed. by Michael Ernst et al., p. 022045. DOI: `10.1088/1742-6596/396/2/022045`.

[24] N. Amin. private communication. 2022.

[25] J. W. Motz, H. A. Olsen, and H. W. Koch. “Pair production by photons”. *Rev. Mod. Phys.* 41 (1969), pp. 581–639. DOI: `10.1103/RevModPhys.41.581`.

[26] Geant4 Collaboration. *Physics Reference Manual, Release 10.4.* 2017.

[27] R. L. Workman et al. “Review of Particle Physics”. *PTEP* 2022 (2022), p. 083C01. DOI: `10.1093/ptep/ptac097`.

[28] N. Foss. “Machbarkeitsstudie zur Analyse von π^0-Mesonen am NA61/SHINE Experiment”. Bachelorarbeit. Karlsruher Institute für Technologie, 2019.

[29] R. Brun et al. “GEANT Detector Description and Simulation Tool” (). DOI: `10.17181/CERN.MUHF.DMJ1`.

[30] R. Ulrich, T. Pierog, and C. Baus. *Cosmic Ray Monte Carlo Package, CRMC.* Version 2.0.1. Aug. 2021. DOI: `10.5281/zenodo.5270381`.

[31] T. Pierog and K. Werner. “Muon Production in Extended Air Shower Simulations”. *Phys. Rev. Lett.* 101 (2008), p. 171101. DOI: `10.1103/PhysRevLett.101.171101`.

[32] S. Ostapchenko. "QGSJET-II: towards reliable description of very high energy hadronic interactions". *Nuclear Physics B - Proceedings Supplements* 151.1 (2006). VERY HIGH ENERGY COSMIC RAY INTERACTIONS, pp. 143–146. DOI: `10.1016/j.nuclphysbps.2005.07.026`.

[33] H. Bethe. "Theory of the Passage of Fast Corpuscular Rays Through Matter". *Annalen Phys.* 5 (1930), pp. 325–400. DOI: `10.1002/andp.19303970303`.

Acknowledgement

I want to express my gratitude towards some persons who supported me during my thesis.

First I would like to thank Prof. Dr. Ralph Engel for the opportunity to write my thesis at the Institute for Astroparticle Physics. Furthermore, I would like to thank Prof. Dr. Ulrich Husemann for his willingness to be my second examiner.

This work would not have been possible without my supervisor Dr. Michael Unger. He discussed all relevant aspects of my topics with me and provided support wherever possible. He especially helped me to find a new topic after the fragmentation run was delayed.

I would like to thank the members of the NA61/SHINE collaboration for their support. Especially, I want to thank those who welcomed me during my stay at CERN.

I am extremely grateful to Neeraj Amin for his continuous support. He was always there to answer my questions and to help me with various problems. I am grateful to Dr. Darko Veberič and Kathrin Bismark for many fruitful discussions. I would also like to recognize Sabine Bucher for the excellent organization of my work trips. I had the pleasure of working with many friendly people at the Institute for Astroparticle Physics.